

HISTORY, CURRENT STATE, AND FUTURE DIRECTIONS OF IONOSPHERIC IMAGING

Gary S. Bust^{1,2} and Cathryn N. Mitchell³

Received 4 September 2006; revised 1 May 2007; accepted 6 August 2007; published 26 February 2008.

[1] With the current data availability from both ground- and space-based sources, the network of ground-based Global Positioning System (GPS) receivers, GPS occultation receivers, in situ electron density sensors, and dual-frequency beacon transmitters, the time is right for a comprehensive review of the history, current state, and future directions of ionospheric imaging. A brief introduction and history of ionospheric imaging is presented, beginning with computerized ionospheric tomography. Then, a comprehensive review of the current state of ionospheric

imaging is presented. The ability of imaging algorithms to ingest multiple types of data and use advanced inverse techniques borrowed from meteorological data assimilation to produce four-dimensional images of electron density is discussed. Particular emphasis is given to the mathematical basis for the different methods. The science that ionospheric imaging addresses is discussed, and the scientific contributions that ionospheric imaging has made are described. Finally, future directions for this research area are outlined.

Citation: Bust, G. S., and C. N. Mitchell (2008), History, current state, and future directions of ionospheric imaging, *Rev. Geophys.*, 46, RG1003, doi:10.1029/2006RG000212.

1. INTRODUCTION

[2] The overall aim of this review paper is to summarize the direction and challenges of an area at the forefront of research: ionospheric imaging. This is the production of two-, three-, and four-dimensional images of the free electron density in the Earth's upper atmosphere.

[3] The ionosphere is the upper region of the Earth's atmosphere where a small but significant number of the neutral atoms are ionized, resulting in free electrons and ions (a plasma). The ionization levels in this near-Earth space plasma are controlled by solar extreme ultraviolet (EUV) radiation and particle precipitation. The dynamics of the neutral atmosphere plays a significant role in causing movement of the ionized particles by collisions with neutral atoms and molecules from the surrounding thermosphere. The ionosphere is embedded within the Earth's magnetic field and thus is constrained by interactions of the ionized particles with the magnetic field. At middle and low latitudes the ionosphere is contained within a region of closed field lines, whereas at high latitudes the geomagnetic field can reconnect with the interplanetary magnetic field

and thus open the ionosphere to the driving force of the solar wind. Introductory texts on the ionosphere are given by *Hargreaves* [1995] and *Davies* [1990].

[4] The physics of the Sun-Earth system poses a number of scientific challenges. Above the Earth's gaseous atmosphere is a fascinating region of complex physics: fluid dynamics, magnetic fields, solar radiation, and particles. Solar storms ultimately have their major terrestrial impact when they encounter the ionosphere through magnetosphere/ionosphere coupling. The physics of the Sun-Earth system is described in detail by *Kivelson and Russell* [1995]. The ionosphere responds to magnetospheric inputs in a number of different ways, with changes in electron and ion temperature, electron and ion and neutral density and mixing of the neutral atmosphere resulting in changes to the ionic species. All of these are important physical parameters, but arguably, the most important is the electron density. Ionospheric imaging of the electron density provides snapshots of the global plasma structure and its temporal evolution. The overall plasma structure and temporal evolution in a large spatial region (such as the polar cap) can be related to important energy and momentum drivers such as variation in the solar magnetic field, changes in the total polar cap potential, hemispheric power, and the amount of energy in the precipitation of electrons and ions from the magnetosphere.

¹Atmospheric and Space Technology Research Associates, San Antonio, Texas, USA.

²Formerly at Applied Research Laboratories, University of Texas at Austin, Austin, Texas, USA.

³Department of Electronic and Electrical Engineering, University of Bath, Bath, UK.

[5] The electron density is certainly the most important parameter from the applications perspective because it governs all of the effects on radio signals. It is this fact that makes ionospheric imaging such a useful technique for radio systems applications; it allows the three-dimensional (3-D) time-evolving (hence four-dimensional (4-D)) spatial field of electron density to be imaged, and this is exactly the requirement for almost all radio systems applications. Measuring changes in the ionosphere, in particular the electron density, is central to understanding the solar-terrestrial environment impact on communication, surveillance, and navigation systems here on Earth. By having an organized 3-D near-global map of electron density updated regularly in time, the radio frequency system user can apply corrections both where and when required. *McNamara* [1991] discusses some of the ionospheric effects on radio systems.

[6] Ionospheric imaging involves using integrated measurements of electron density, known as total electron content (TEC) measurements, to produce two-, three-, and four-dimensional maps of electron density. Most of the basic TEC measurements are obtained from networks of geodetic Global Positioning System (GPS) receivers that measure the ionosphere in order to improve the accuracy of their position calculations. These TEC measurements can be used directly or organized into two-dimensional (2-D) TEC maps to infer information on the horizontal structuring of the electron density. However, information on how plasma can be lifted to high altitudes and transported to other regions, polar outflow, and other vertical dynamical changes is lost with such simple mapping algorithms. In order to obtain information on the vertical structure of the electron density, its temporal variation, and transport, 4-D imaging is necessary. Ionospheric imaging to obtain electron density is complementary to using point profiles from ionosondes and incoherent scatter radars (ISRs). For the point profiles, there is no information about large-scale horizontal gradients and convection of plasma that causes structuring at the profile position. The time-evolving nature of 4-D imaging is crucial since for most raw satellite TEC data used in the imaging the temporal and spatial sampling within a given region is constantly changing. Moreover, the ionospheric conditions, electron density in particular, can significantly change with space and time. With 4-D imaging, there is the capability to understand how plasma structures evolve in time and how they affect local smaller-scale plasma structuring.

[7] The paper is organized as follows: Section 2 describes the theoretical underpinnings and historical developments of two-dimensional ionospheric tomographic imaging, including a short tutorial on computerized tomography. Section 3 is focused on 3-D and 4-D ionospheric imaging. The mathematical development of 3-D imaging methods is presented for several different approaches, including those that make use of data assimilation techniques. Early results and experimental validation of 2-D and 3-D imaging is presented in section 4, while section 5 focuses on recent scientific results of 4-D imaging at high, middle, and low latitudes. Application results and developments of 4-D imaging are presented in section 6. Finally, a summary

and discussion of future directions of research and development for 4-D imaging is presented in section 7.

2. THEORY: TWO-DIMENSIONAL IMAGING

2.1. Introduction to Tomography and Ionospheric Tomography

[8] The mathematical problem of reconstructing a function from its projections was originally solved by *Radon* [1917]. However, the first practical application was not published until 1956, when the tomographic method was applied to radio astronomy [*Bracewell*, 1956].

[9] The strict definition of tomography reflects its derivation from the Greek words “to cut or section” (tomos) and “to write” (graphein), hence the use of the term for obtaining 2-D pictures of the interior of the body from integrated measurements. The use of tomography has now broadened to cover a wide range of 2-D and 3-D inverse problems that originate with multiangle measurements that relate to the interior of the object.

[10] Tomography is an example of an inverse problem, where imaging of a particular quantity is performed from diverse measurements. The technique has many applications and is found in many different areas of science such as archaeology, biology, geology, and, the best known example, in medicine. The recent interest in tomographic imaging began with the invention of the X-ray computerized tomography scanner by *Hounsfield* [1972]. This original medical application, the computer-aided tomography (CAT) scanner, took measurements of the attenuation of X rays passing through a human body from many different angles. By converting these measurements directly into digital impulses and feeding them into a computer, a two-dimensional, cross-sectional image of the body was obtained. In modern computed tomography a three-dimensional image of a body and its internal organs is formed from a series of two-dimensional X-ray images. More recent developments in the medical field have seen the technique applied to nuclear medicine, magnetic resonance imaging, and ultrasound and microwave imaging. Further information about tomographic imaging is given by *Kak and Slaney* [2001].

[11] The application of tomography to imaging the electron density in the ionosphere falls into the category of ray tomography. It has the advantage that the measurements can be approximated as straight-line integrals of the electron density, and it is therefore not necessary to construct an algorithm to cope with ray bending, which only introduces a few kilometer path difference for GPS, for horizontal occultations [*Schreiner et al.*, 1999]. On the other hand, the measurements are compromised by the incomplete geometrical coverage and by assumptions of stationarity of the medium. While both of these limitations have been addressed in the last few years and improvements have been achieved, they remain important considerations in ionospheric imaging.

[12] The number of free electrons in a column (defined as of unit cross-sectional area) from the satellite (S) to the receiver (R) is the slant TEC along the path. This TEC can

be determined from the differential phase [see, e.g., *Davies, 1990*] of dual-frequency satellite transmissions, but in that case it contains an unknown constant, c , because of the unknown number of differential phase cycles at the start of the measurement. This measured TEC is related to the true slant TEC by

$$y_s = \int_s^R N ds + c, \quad (1)$$

where y_s is the measured TEC along the path, N is the electron density, ds is the differential distance along the path between satellite and receiver, and c is an unknown constant. TEC is the basic measurement used in ionospheric imaging, and it is important to appreciate that the algorithms always have to manage the TEC calibration (the determination of the constant) in some manner. For GPS imaging this can be assisted by using the differential code technique, where the code data [see, e.g., *Mannucci et al., 1999*] give an absolute signal delay and hence absolute TEC but include satellite- and receiver-specific interfrequency biases (IFB). Fortunately, the IFB values are relatively stable [*Mannucci et al., 1999*] and not dependent on the ionosphere. This is not the case for the unknown number of differential phase cycles at the start of the measurement, which is ionosphere-dependent and hence unique for each measurement arc. Thus, for GPS, estimates of the IFBs can be obtained by taking models of the ionosphere (empirical or from 2-D to 4-D imaging) and computing average values of the IFB over several hours. However, any systematic errors in the ionosphere models will produce errors in the IFB value estimations [*Juan et al., 1997*].

2.2. Data Sources

[13] Tomography algorithms that were developed for imaging the ionosphere with TEC data from polar-orbiting satellites recorded at multiple ground-based receivers are described in section 2.3. The satellites are in either the Russian Cicada system or the Navy Navigation Satellite System (NNSS) that later became known as the Navy Ionosphere Monitoring System (NIMS). These satellites are low-Earth-orbiting (LEO) satellites with the satellite altitudes approximating 1100 km. They broadcast two coherent frequencies at nominal values of 150 and 400 MHz. Owing to their LEO orbit the ionosphere can often (but not always) be considered temporally static during a satellite pass.

[14] Later, the development of global, three-dimensional, time-varying algorithms made use of the GPS constellation of satellites as data sources. The GPS constellation is in a 55° inclination, with 24 or more active satellites. For a given receiver location, at any time, between 8 and 12 satellites are in view. The GPS satellites are at an altitude of $\sim 20,000$ km and broadcast at frequencies of ~ 1.2 and ~ 1.6 GHz. With GPS, true 3-D time-evolving tomographic imaging becomes possible.

[15] With LEO TEC data from NIMS or Cicada a rich set of data is available along the track of the satellite for rays between the satellite and ground array of receivers. The ionosphere can be considered static, and a 2-D tomographic image can be produced along the satellite track. However, the 2-D image is necessarily regional ($\sim 10^\circ$ in horizontal distance), and the images are only produced when satellites pass over the array. For a midlatitude site, four NIMS satellites (the current number available) produce ~ 10 passes per day to a receiver array. Thus traditional 2-D LEO tomography is limited both spatially and temporally. GPS, on the other hand, continuously provides TEC data to a ground receiver from multiple satellites. However, the satellites move slowly through the ionosphere (~ 100 m/s at F region altitudes). Thus, in order to develop global 3-D images of electron density, large numbers of ground GPS receivers are required, and some method of accounting for temporal evolution of the ionosphere must be included in the imaging algorithm. Modern 4-D imaging algorithms have developed methods to account for both of these issues. Finally, the radio frequencies used by GPS and LEO systems can have an effect on the fidelity of the imaging. During severe magnetic storms in regions of strong scintillation, receivers often lose lock at 150 MHz, causing data dropouts that can last for several hours. In addition, at lower-elevation angles, bending at 150 MHz can become an important effect. Both of these effects reduce the effectiveness of LEO tomography, particularly during severe magnetic storms.

[16] Recently, GPS receivers on LEO satellites have provided new data sources that have been added to 4-D tomographic imaging algorithms. GPS occultation TEC comes from rising or setting occultations and provides the horizontal ray information that is not available from angle-limited ground-based tomography, while dual-frequency navigation receivers provide upward looking TEC data and allow for improved 4-D imaging of the topside ionosphere and plasmasphere.

2.3. Developing Theory

[17] The first research work in ionospheric tomography was done by *Austen et al.* [1988]. They set up a computer simulation study in which the electron density lay within a piecewise-constant grid oriented along a latitude-altitude plane of constant longitude. TEC values were computed for a realistic satellite-receiver configuration by integration along specified raypaths through their electron density model. They then reconstructed the electron density distribution using a finite series expansion reconstruction technique. The algorithm choice was based on work by *Censor* [1983], since such methods can be used with any raypath geometry and are often the preferred option when the line integral data have been collected over a limited range of orientations. As an initial condition for the algorithm the authors used a triangular vertical density profile with a peak density close to that of the model used in the simulation. The simultaneous iterative reconstruction technique (SIRT) algorithm, a development of the least squares algebraic

reconstruction technique (ART), was used to reconstruct the image. ART is described in section 2.3.2.

[18] Another iterative algorithm was introduced by *Raymund et al.* [1990]. They describe the application of the multiplicative algebraic reconstruction technique (MART) algorithm to ionospheric tomography. They used a simulation study similar to that of *Austen et al.* [1988]. MART is an entropy-optimization algorithm that was proposed by *Gordon et al.* [1970]. It is considered a suitable algorithm to use in situations where the data are incomplete. To produce an initial starting condition for the algorithm, TEC along a satellite-to-receiver raypath is considered to be divided between the pixels that the raypath intersected, with the proportion of TEC assigned to a pixel distributed according to the length of the raypath within that particular pixel. An electron density value was obtained by dividing the assigned TEC by the intersection length. This procedure, a form of back projection, was combined with a Chapman profile (described by *Hargreaves* [1995]) weighting to assign the initial electron densities for the algorithm. The reconstructed images indicated that good agreement with the original simulations could be achieved using this method.

[19] Now that the feasibility of ionospheric tomography had been demonstrated, the focus turned to limitations of the new technique. *Yeh and Raymund* [1991] investigated some of the theoretical limitations of ionospheric tomography. They noted that the sphericity of the Earth imposes a limitation to the lowest elevation of a raypath, and therefore near-horizontal TEC measurements through the ionosphere are not available. This poses a restriction on the ability to reconstruct the vertical profile in electron density. In addition, refraction of the radio wave at low elevations limits the accuracy of the TEC values obtained from such rays. A further limitation to the accuracy of the images occurs because of the discrete locations of the receivers. The temporal variation of the ionosphere during the data collection period was also noted, and for future work the implementation of a time-dependent algorithm was suggested. This idea could be used with experimental measurements during ionospheric conditions where the assumption of an unchanging ionosphere for the duration of the satellite pass (10–20 min) breaks down. This has been adopted for later work on 3-D imaging with GPS data [*Mitchell and Spencer*, 2003].

[20] *Raymund et al.* [1994] ran simulation studies using the mathematical technique for least squares fitting known as singular value decomposition (SVD) to produce a tomographic image from a linear combination of model ionospheres. A number of ionospheres given by the fully analytic ionospheric model were considered, and SVD was used to select a linear combination of these model ionospheres. However, small-scale structures are not represented in these ionospheric models, and hence no combination of the models could reproduce detailed images. A development of the method was necessary where the selected combination of models was used as the initial condition (background ionosphere) showing the large-scale

features, and an iterative algorithm was then used to add in the detail [*Raymund et al.*, 1993]. This two-stage method, involving the selection of the initial condition from models followed by the MART algorithm, has been extensively used in experimental ionospheric tomography by researchers at the University of Wales, Aberystwyth. The two-stage technique is now described in more detail here. The first stage, selection of initial conditions from models, is first described in section 2.3.1. Then the second-stage iterative algorithms ART and MART are discussed.

2.3.1. Background Ionosphere

[21] In iterative algorithms the compensation for the incomplete information in the measurements is made through the use of a starting point for the algorithm, known as a background ionosphere. In this case it is chosen to be the best guess that can be made before the measurements are introduced. To make this guess, an empirical model of the ionosphere such as the international reference ionosphere (IRI) is chosen. Then, 24 different specifications of the electron density are made by running the model for a range of 24 discrete times around the time of measurements. Each electron density model represents the ionosphere at the resolution of the tomographic grid, at discrete time intervals over a variable time period, centered on the time of the satellite pass. It is assumed that the matrix of electron density in the background ionosphere, \mathbf{x}_0 , can be expressed as a weighted sum of the 24 models, $\tilde{\mathbf{X}}$, where

$$\mathbf{x}_0 = \tilde{\mathbf{X}}\tilde{\mathbf{W}} \quad (2)$$

and where $\tilde{\mathbf{W}}$ is a vector of the 24 weighting coefficients that are to be found. Each column of matrix $\tilde{\mathbf{X}}$ represents a particular model. In each row an element represents an electron density in a specific ionospheric locality, defined by a pixel of uniform electron density. Let $\tilde{\mathbf{H}}$ be a matrix describing the geometry of the raypaths with respect to the grid, containing the path lengths of each ray in each pixel. The TEC values along the raypaths through the background ionosphere \mathbf{y}_0 are given by

$$\mathbf{y}_0 = \tilde{\mathbf{H}}\mathbf{x}_0 = \tilde{\mathbf{H}}\tilde{\mathbf{X}}\tilde{\mathbf{W}}. \quad (3)$$

[22] The matrix product $\tilde{\mathbf{H}}\tilde{\mathbf{X}}$ can be represented by a matrix $\tilde{\mathbf{M}}$, which contains calculated TEC values along satellite-to-receiver raypaths through each of the model ionospheres. The matrix $\tilde{\mathbf{M}}$ consists of 24 column vectors, one for each model. The number of column vectors was chosen initially to have a model from each hour in the day. Each row is for a satellite to receiver raypath. The measured TEC values, \mathbf{y} , are assumed to be equal to a linear combination of these model TEC values, so

$$\mathbf{y} = \tilde{\mathbf{M}}\tilde{\mathbf{W}}. \quad (4)$$

[23] The least squares solution to $\tilde{\mathbf{W}}$ was then computed using SVD to find the pseudoinverse, and

$$\tilde{\mathbf{W}} = (\tilde{\mathbf{M}})^{-1}\mathbf{y}. \quad (5)$$

[24] The background ionosphere is then formed from equation (2). Once a background ionosphere is formed from the linear combination of models, an iterative algorithm is run to add the finer-scale features to the image. The iterative algorithms are described in sections 2.3.2 and 2.3.3. In the description of iterative algorithms the notation changes to refer to individual pixels rather than matrices of the entire pixel grid. This is because iterative algorithms work recursively on individual pixels.

2.3.2. Algebraic Reconstruction Technique

[25] The ART algorithm was first published by *Gordon et al.* [1970]. Rather than trying to handle a given system of equations as a whole, the ART works by an iterative process and has been shown to converge to the least squares solution. ART has been published with several modifications. The one described here is the ART algorithm with relaxation from *Censor* [1983]. An initial guess, x_j^0 , is obtained from the background ionosphere and for the $k + 1$ th iteration

$$x_j^{k+1} = x_j^k + \lambda_k \frac{y_i - \sum_{m=1}^n \Delta_{im} x_m^k}{\sum_{m=1}^n \Delta_{im} \Delta_{im}} \Delta_{ij}, \quad (6)$$

where λ_k , the relaxation parameter, is a number or series of numbers used to control the convergence of the algorithm, Δ_{ij} is the length element of raypath i through pixel j , im is the loop over m from 1 – n for each i , and n is the total number of pixels in the grid. The current iterate, x_j^k , is refined to a new value, x_j^{k+1} , by considering a single ray, i , and changing the electron density value of the pixels, j , intersected by the ray. The discrepancy between the measured TEC and the TEC calculated through the current image is then redistributed among the pixels along the ray in proportion to the length of intersection with each pixel Δ_{ij} . The algorithm then cycles through all raypaths several times until convergence is achieved.

[26] The ART algorithm has been successfully implemented in experimental ionospheric tomography by *Andreeva* [1990] and *Kunitsyn et al.* [1994a, 1994b, 1995]. The SIRT algorithm is a development of the ART algorithm, where the first update to the density is made after all of the raypaths have been considered once, i.e., after one iteration. The SIRT algorithm has been used in ionospheric tomography by *Pryse et al.* [1993].

2.3.3. Multiplicative Algebraic Reconstruction Technique

[27] The MART algorithm was originally proposed as a reconstruction algorithm by *Gordon et al.* [1970] and was later proven to converge to the maximum entropy solution by *Lent* [1997]. The maximum entropy solution means that the function

$$f(x) = - \frac{1}{\ln(n^2) \sum_{j=1}^n x_j} \ln \frac{x}{\sum_{j=1}^n x_j} \quad (7)$$

will be maximized. The maximum entropy approach to image reconstruction yields the image with the lowest information content that is consistent with the available measurements [*Menerbo*, 1979]. This reduces the tendency to introduce artifacts into the image region. *Censor* [1983, p. 414] notes that B. R. Frieden, writing about image restoration, stated “the most likely object scene implied by given image data is found to obey the principle of maximum entropy.” *Censor* suggests that this could also be applied to image reconstruction.

[28] The initial application of this algorithm to experimental ionospheric tomography was by *Raymund et al.* [1990], although in an experimental situation with noise on the data the behavior of the MART algorithm is not well understood. In particular, its response to inconsistent sets of equations is unknown [*Censor*, 1983]. Nevertheless, the MART algorithm has been used successfully for the reconstruction of tomographic images of the ionosphere by several authors [*Kersley et al.*, 1993; *Heaton et al.*, 1995; *Mitchell et al.*, 1995; *Pryse et al.*, 1995; *Vasicek and Kronschnabl*, 1995].

[29] The MART algorithm, as in the case of ART, requires an initial starting value for each pixel, x_j^0 for $j = 1, \dots, n$, and in the case of ionospheric tomography this is the electron density in the background ionosphere. The algorithm then updates the electron density in the image region according to the formula

$$x_j^{k+1} = x_j^k \left(\frac{y_i}{\sum_{j=1}^n \Delta_{ij} x_j^k} \right)^{\frac{\lambda_k \Delta_{ij}}{\max \Delta_j}}. \quad (8)$$

Thus for each TEC measurement a multiplicative correction is made to the electron density of every pixel. The relaxation parameter, λ_k , which controls the convergence of the algorithm, is bounded to lie between 0 and 1.

2.4. Other Early Methods and Image Resolution

[30] A number of noniterative algorithms have been applied to ionospheric tomography. These are mathematically similar to the creation of the background ionosphere described previously, with some modifications to allow smaller features to be imaged.

[31] *Na and Lee* [1990] applied an orthogonal decomposition technique in which they generated a set of Fourier orthonormal basis functions from a priori information. Each was derived from a different frequency component and orientation. The tomographic image could then be formed from a combination of these basis functions. A further publication [*Sutton and Na*, 1994] tested this approach to the reconstruction using simulated data and produced some promising results. However, *Sutton and Na* noted the significant reliance of the vertical profile in the reconstruction on a priori information. This problem was not only found with their method; in fact, it is a consequence of the lack of complete data coverage [e.g., *Cornely*, 2003].

[32] *Fremouw et al.* [1992] used a set of vertical orthonormal vectors, created from ionospheric models, to image the vertical profile and a power law spectrum to select the horizontal structures from a Fourier basis. This approach has proven to be highly successful and has been used subsequently in various modified forms by a number of researchers. A new algorithm, described by *Raymund et al.* [1994], was similar to the technique used by *Raymund et al.* [1994], but the solution was no longer constrained to lie in the subspace of ionospheric models, and it satisfied the TEC values completely. However, the solution was not unique, and forcing the solution to match an ionospheric model in a least squares sense finally resolved the ambiguity in the solution. However, this initially promising algorithm never showed a significant improvement over other computationally less expensive methods.

[33] *Fougere* [1995] pursued a novel approach in which a range of Chapman profiles were used to form an orthonormal set and were incorporated into the reconstruction in the form of horizontal rays. The solution to the modeled TEC was then computed using a maximum entropy algorithm. The method was not tested on any model representative of the ionospheric electron density, but several test simulations showed that excellent reconstructions of Gaussian enhancements could be achieved, even with the geometrical constraints imposed by ionospheric tomography.

[34] *Kuklinski* [1997] set up a three-dimensional image grid in longitude, latitude, and altitude providing voxels (a voxel is a 3-D pixel and can be in any coordinate frame) of size $0.5^\circ \times 0.5^\circ \times 45$ km. TEC measurements, recorded during the Russian-American tomography experiment (see section 4), were then used to reconstruct a tomographic image in the plane defined by the receiver chain and the satellite orbit. *Kuklinski* [1997] also presented simulation results, employing a network of some 50 receivers spread over the United States, indicating the possibility of quasi-three-dimensional ionospheric images from a single NNSS satellite pass. In 1997, *Mitchell et al.* [1997a] showed experimental results that realized a simplified version of this idea, where two chains of NNSS receivers were deployed in Scandinavia.

[35] *Na and Sutton* [1994] investigated the resolution limits of ionospheric tomography. They separated their analysis into projections and considered the case of the 3-dB resolution of two structures within the ionosphere. They found that the resolution improved as the density of receivers increased but that a limit of around 50 km was found. This is apparently consistent with experiments since it is smaller than the smallest verified features imaged in the ionosphere using tomography [e.g., *Mitchell*, 1997b]. Subsequent work on the resolving capabilities of different geometries [*Na and Sutton*, 1994; *Na et al.*, 1995] has allowed the theoretical resolutions of different ionospheric tomography experiments to be assessed. *Heaton et al.* [1995] tested the incorporation of scaled ionograms into the imaging, and this resulted in some improvement in the vertical profiles. The determination of vertical profiles was investigated in some detail, in the experimental environment

over Scandinavia, by *Mitchell et al.* [1997c]. They used a series of Chapman profiles to describe the vertical electron density profile and found that while the peak height could often be determined to within about 30 km, the scale height and peak density relationship was ambiguous; a larger scale height and lower peak density could often fit the original TEC data as closely as a smaller scale height and higher peak density.

3. THEORY: THREE-DIMENSIONAL IMAGING

[36] *Hajj et al.* [1994] first discussed the potential of using ground- and spaced-based GPS observations to image the ionosphere. They suggested the satellite-to-satellite transmission of GPS to LEO dual-frequency L band signals to provide the vertical structure, with ground-based receivers recording from NNSS satellites providing the horizontal structure. They indicated that the GPS-LEO measurements would be of particular help in defining the *E* layer and that these additional measurements could provide information for either two- or three-dimensional reconstructions. In a subsequent publication, *Leitinger et al.* [1997] outlined the possibility of using data from the first radio-occultation satellite GPS/MET to complement ground-based NNSS tomography.

[37] *Rius et al.* [1997] showed the first experimental results that used GPS data to image the ionosphere. Although their vertical grid consisted of just four height voxels, this was a key step in the transition from 2-D mapping [*Wilson et al.*, 1995; *Mannucci et al.*, 1999] and intermediate multiple shells [*Juan et al.*, 1997] into 3-D imaging. They used a Kalman filter approach to accommodate temporal changes in the images. Kalman filters have been used for numerous engineering applications where the state of a dynamic system is to be estimated from incomplete measurement data. The approach exploits knowledge of the evolution of the system to reduce the noise or to interpolate missing data. In data assimilation [see *Daley*, 1991] the Kalman filter uses the map and error covariances from the previous time step as the background model and error covariances for the present time step. *Howe et al.* [1998] applied the Kalman filter approach to ionospheric tomography. This combined and extended ideas from the vertical-slice ionospheric tomography work of *Fremouw et al.* [1992] and the 2-D horizontal mapping of GPS TEC [*Wilson et al.*, 1995] into a full three-dimensional algorithm. An outline of the general approaches to three-dimensional imaging of the ionosphere is given in section 3.1.

3.1. Three-Dimensional Ionospheric Imaging

[38] Imaging in three dimensions is essentially the same as in two dimensions, but some complications have to be overcome because of the sparseness of the data coverage. For that reason, iterative pixel-based methods (such as ART or MART) are not chosen, since they do not couple the changes applied to one voxel across to other voxels that may have no intersections with measurements. Nevertheless, the electron density field is discrete for at least part of

each imaging method. In some cases [e.g., *Howe et al.*, 1998] the field can be changed into functional form for part of the inversion procedure. In general, a three-dimensional grid of voxels is defined, each bounded in latitude, longitude, and altitude. Several authors have chosen Sun-fixed coordinates [e.g., *Juan et al.*, 1997] exploiting the solar EUV dominance of the ionization that can help to fill data gaps. Others have preferred a general geographic frame [e.g., *Mitchell*, 2002] since they often aim to image the disturbed ionosphere, which does not follow simple EUV-dominated changes.

[39] As for the 2-D case the length of each straight-line element of a satellite-to-receiver signal propagation path though each intersected voxel is computed from knowledge of the satellite and receiver locations. The unknown electron concentration is defined to be constant within each voxel and contained in the column vector \mathbf{x}_a . This can be expressed as

$$\mathbf{y} = \tilde{\mathbf{H}}\mathbf{x}_a, \quad (9)$$

where the matrix $\tilde{\mathbf{H}}$ transforms the electron density to the form and location of the observations and \mathbf{y} are the observed TECs.

[40] There are several approaches to using the observed TECs. The simplest conceptually is to calibrate the TEC observations before using them into the inversion. For GPS data this can be achieved by using both the differential phase and the differential delay data and correcting for the satellite and receiver interfrequency biases. While the original estimates for the accuracy of interfrequency biases were a few TEC units, recent work by *Ciraolo et al.* [2007] shows that much larger errors can be found. Consequently, this approach should be undertaken with care, and consideration for possible errors must be given, especially when using such data in assimilation algorithms where the estimate of measurement error is critical to the solution.

[41] An alternate approach is to use the relative changes of TEC along continuous satellite-receiver paths. If this route is taken, then the inversion algorithm must calibrate the unknown constants, as was the case for the 2-D algorithms of *Andreeva* [1990]. In this case the problem is analogous to that of using NNSS data: Differential phase arcs are used, and the inversion uses relative differential phase observations. Thus appropriate lines of, first, the geometry matrix, $\tilde{\mathbf{H}}$, then the measurement matrix, \mathbf{y} , are differenced, such that measurements along continuous satellite-receiver arcs are taken relative to a certain reference measurement within that arc.

[42] Equation (9) cannot be used directly to find the electron density \mathbf{x}_a because the measurement geometry is not ideal. The inversion system is underdetermined. Many approaches exist to compensate for the missing information to allow the reconstruction of a spatially continuous electron density field. Mathematically based constraints can be applied to obtain a physically reasonable solution. One approach to applying the constraints is to form a basis set of orthogonal functions that are formed from empirical or

physical models. These functions will then allow the reconstruction of the ionosphere. This empirical orthogonal function (EOF) approach was taken by *Fremouw et al.* [1992]; the extension into 3-D GPS imaging with a Kalman filter was first shown by *Howe et al.* [1998]. A time-dependent extension of this technique without a Kalman filter, where the electron density is allowed to vary linearly in each voxel over a period of an hour, was shown by *Mitchell and Spencer* [2003].

[43] A set of 3-D orthonormal basis functions is defined in accordance with the geophysical conditions and data coverage. For example, horizontally, these could be pixels, spherical harmonics, or wavelets. Vertically could be any orthogonal basis set formed from empirical or mathematical models. The time, location, and geophysical conditions can be used to tailor specific EOFs [e.g., *Materassi and Mitchell*, 2005a, 2005b] and truncation of the spherical harmonics to minimize aliasing in data-sparse regions [Mitchell and Spencer, 2003]. A mapping matrix, $\tilde{\mathbf{X}}$, is used to transform the problem. This results in a situation where the unknowns are coefficients of 3-D orthonormal basis functions. The combination of these will give the final image of electron concentration. The horizontal functions provide a flexible basis to determine the horizontal distribution of ionization, which is generally well specified by the data; the EOFs form a constraint to the underdetermined vertical profile.

[44] This can now be expressed mathematically as

$$\mathbf{y} = \tilde{\mathbf{H}}\tilde{\mathbf{X}}\tilde{\mathbf{W}}, \quad (10)$$

where the matrix $\tilde{\mathbf{X}}$ contains the basis functions. $\tilde{\mathbf{H}}\tilde{\mathbf{X}}$ now represents the set of modeled TEC that are formed by integration through the set of 3-D basis functions. Applying a matrix inversion, for example, using singular value decomposition, the inversion can be performed such that

$$\tilde{\mathbf{W}} = (\tilde{\mathbf{H}}\tilde{\mathbf{X}})^{-1}\mathbf{y}, \quad (11)$$

and the solution to the inverse problem is then given by applying the matrix of “weights” back to the 3-D basis functions,

$$\mathbf{x}_a = \tilde{\mathbf{W}}\tilde{\mathbf{X}}. \quad (12)$$

[45] The algorithm can be extended into a time-dependent inversion by incorporating a priori information about the evolution of the electron concentration during a specified period of time. If the change electron concentration within a voxel with time is linear, then it is possible to write the same system of equations to solve for the change in the relative contributions of each basis function [Mitchell and Spencer, 2003].

3.2. Data Assimilation Approaches

[46] Another approach to three-dimensional, semicontinuous imaging of plasma density is data assimilation, as practiced in oceanography and meteorology. The similarity

between meteorology and space weather has led a number of researchers to discuss the idea of applying meteorological forecasting techniques to ionospheric forecasting. Daley [1991] provides a comprehensive treatment of the theoretical foundations of data assimilation for numerical weather forecasting. While the objective of full data assimilation is to operationally specify and forecast the state of the ionosphere, such methods can also be used to produce 4-D images of ionospheric electron density, which is the main interest in this review. Below we present a brief discussion of ionospheric data assimilation and provide examples of the main techniques that have been developed for ionospheric data assimilation. The goal here is present ionospheric data assimilation within the context of 4-D imaging. Thus a full derivation and exposition of data assimilation methods is beyond the scope of this review. The interested reader can obtain a more complete discussion from the many references provided.

[47] True data assimilation is fundamentally a model specification and prediction technique that uses data to improve the fidelity of the model. For the ionosphere the relationship between raw input data and resulting images of electron density is complex. It is based on first-principles physics models that typically consist of multiple species of ions and neutrals, each with its own continuity, momentum, and energy equations and all coupled to Maxwell's equations. The resulting electron density specification is dependent upon the numerical model itself; that is, the resulting 4-D electron density field is influenced by both the underlying numerical model and the inputs that drive it. In contrast, with 4-D imaging the relationship (or forward model) between the state variable to be imaged (ionospheric electron density) and the observations is simple. For example, in tomographic imaging the forward model is a path integral over the quantity to be imaged. Thus in tomography, there may be no physics model, though regularization through mathematical techniques is often used to provide necessary a priori information along with networks of data to create the image.

[48] In data assimilation, there are four stages: (1) Collect the data to be assimilated and do quality control on the data. (2) Organize the data into 3-D (or 4-D) maps of the state variable being assimilated through an "objective analysis" technique, using the current best model forecast of the state variable. (3) Reinitialize the state variables in the first-principle model being used and (if desired) estimate the inputs to the model from the objective analysis. (4) Using the newly initialized model, forecast forward to the next data assimilation time.

[49] Stage 1 is not discussed further in this review since it is an essential step for all data analysis. The output of stage 2 at a given time includes a 3-D estimation or image of electron density. Thus any data assimilation algorithm that includes stage 2 results can be used for 4-D imaging. Stages 2 through 4 have been implemented in three separate algorithms discussed in detail below. Applied Research Laboratories, University of Texas at Austin has developed the ionospheric data assimilation three-dimensional

(IDA3D) algorithm. IDA3D produces an objective analysis "map" of the 3-D electron density field that is projected forward in time through a Gauss-Markov Kalman filter. It represents an implementation of stages 2 and 4. Utah State University (USU) has developed the Global Assimilation of Ionospheric Measurements (GAIM) algorithm, which is a first-principles physics-based Kalman filter approach that incorporates stages 2, 3, and 4. The Global Assimilative Ionospheric Model (GAIM) was developed by the University of Southern California and Jet Propulsion Laboratory (USC/JPL) and is an algorithm that also incorporates stages 2, 3, and 4 but in a different manner. Both the USU and USC/JPL GAIM models have Gauss-Markov implementations similar to IDA3D. The Gauss-Markov Kalman filter approach is outlined below. IDA3D is used to demonstrate the mathematical form of the solution. The two GAIM Gauss-Markov Kalman filters have similar mathematical forms.

[50] IDA3D [Bust *et al.*, 2000, 2004] organizes the data into spatial maps of electron density via an objective analysis technique. These spatial maps are projected forward in time through a Gauss-Markov Kalman filter where they are used to initialize the next analysis. However, while the background model can be a first-principles ionospheric model, there is no feedback of the spatial maps into the first-principle model, and no correction or update to the model is made. IDA3D is an objective analysis algorithm (step 2 in the data assimilation cycle above), based upon three-dimensional variational (3DVAR) data assimilation [Daley and Barker, 2001; Daley, 1991]. The basic idea is to create a procedure for combining a model output with actual measurement data. Obviously, sparsely measured quantities could create discontinuities if they were used by directly placing them into a model output. In addition, instruments will measure a quantity over a given region of space, and this measurement in itself will have a region over which it can be considered. The 3DVAR is a statistical minimization procedure that deals with these issues. It takes into account data, data error covariances, a background model, and the background model error covariances.

[51] Following the previous notation in this paper where appropriate, \mathbf{y} is the vector of observations, $\tilde{\mathbf{R}}$ is the error covariance matrix for the observations, \mathbf{x}_f is the forecast (or prediction) model, and $\tilde{\mathbf{P}}_f$ is the error covariance matrix for the forecast model. For a given background forecast (or prediction) the method computes \mathbf{x}_a , which is the analysis electron density at a given time, and the analyzed error covariance $\tilde{\mathbf{P}}_a$. The 3DVAR (or Kalman gain) solution is given as

$$\mathbf{x}_a = \mathbf{x}_f + \tilde{\mathbf{P}}_f \tilde{\mathbf{H}}^T [\tilde{\mathbf{R}} + \tilde{\mathbf{H}} \tilde{\mathbf{P}}_f \tilde{\mathbf{H}}^T]^{-1} [\mathbf{y} - \tilde{\mathbf{H}} \mathbf{x}_f] \quad (13)$$

$$\tilde{\mathbf{P}}_a = \tilde{\mathbf{P}}_f - \tilde{\mathbf{P}}_f \tilde{\mathbf{H}}^T [\tilde{\mathbf{R}} + \tilde{\mathbf{H}} \tilde{\mathbf{P}}_f \tilde{\mathbf{H}}^T]^{-1} \tilde{\mathbf{H}} \tilde{\mathbf{P}}_f, \quad (14)$$

where superscript T is the transpose of the matrix. The analyzed density and error covariance are forecast to the next time step by application of the Gauss-Markov Kalman filter technique [Gelb, 1974]:

$$\mathbf{x}_f(t_{n+1}) = e^{-\frac{\Delta t}{\tau}}[\mathbf{x}_a(t_n) - \mathbf{x}_b(t_n)] + \mathbf{x}_b(t_{n+1}) \quad (15)$$

$$\tilde{\mathbf{P}}_f(t_{n+1}) = \left(1 - e^{-\frac{2\Delta t}{\tau}}\right)\tilde{\mathbf{P}}_b(t_n) + e^{-\frac{2\Delta t}{\tau}}\tilde{\mathbf{P}}_a(t_n), \quad (16)$$

where t_n is time associated with the analysis and model estimates and τ is the decorrelation time. The background model state (empirical or first principle model) is given by \mathbf{x}_b , and its error covariance is given by $\tilde{\mathbf{P}}_b$.

[52] The value of the resulting specifications is dependent upon the amount, the distribution, and the quality of the observations. Any observation that can be predicted from the background model can be ingested. Typically, ingestion is limited to data types that can be predicted without major assumptions or complex calculations. To solve equations (13) and (14), IDA3D needs certain inputs, including background climatology with a model grid, electron density specification, correlations, and a set of observations (direct measurements or radiances from remote sensing) that is easily related to the electron density. The model grid is an input that is chosen for its compatibility with the specific scientific investigation that is planned. Typically, the IRI [Bilitza, 2001], or a first-principle model such as the thermosphere-ionosphere-mesosphere-electrodynamics general circulation model [Roble and Ridley, 1994], is used as the background model. The impact of the background model is significantly reduced by application of the Gauss-Markov Kalman filter technique (equations (15) and (16)). The background model error correlations are treated as inputs that are independent of the background model. At present the correlations are treated as correlation lengths in latitude, longitude, and altitude. The background model correlations decrease exponentially as the ratio of the distance between the model points and the correlation length. The horizontal and vertical distances are treated separately. In addition, a correlation time, τ , is given as input. These correlations allow the data to impact a larger region of the specification than just of the grid points affected by the observations and allow past observations to impact the present specification. Using these techniques, IDA3D is able to ingest any available observation of electron density or electron content.

[53] IDA3D is primarily used as a 3-D electron density imaging algorithm. It is a mature algorithm. It has been validated [Coker et al., 2001; Watermann et al., 2002] and applied to several scientific investigations [Bust et al., 2000; Bust and Crowley, 2007; Yin et al., 2006; Garner et al., 2006; Crowley et al., 2006].

[54] For the last several years, Utah State University has been developing the Global Assimilation of Ionospheric Measurements (GAIM) model [Schunk et al., 2004; Schunk et al., 2005a, 2005b; Scherliess et al., 2004]. GAIM is a data assimilation model that specifies and forecasts the state

of the ionosphere. There are several versions of GAIM under development at USU. One version, a Gauss-Markov Kalman filter [Schunk et al., 2004] is identical to IDA3D in the mathematical derivation and form of the estimation solution. The Gauss-Markov version of GAIM uses the Ionosphere Forecast Model [Schunk et al., 1997] as the background model specification. The Gauss-Markov version of GAIM is currently used operationally at the Air Force Weather Agency. The USU Gauss-Markov version of GAIM has been validated against independent measurements TEC and peak densities from ionosondes [Thompson et al., 2006]. A second version of GAIM being developed by USU is a physics-based, reduced-state Kalman filter assimilation algorithm [Scherliess et al., 2004]. There are two basic ideas. First, computing the full analyzed error covariance (number of grid points squared) is a computationally prohibitive task. So, a reduced-state error covariance is calculated. In practice, the number of grid points in the global ionosphere is reduced to $\sim 1\%$ of the original full grid, reducing the computational requirements by a factor of 10,000. Second, the evolution in time of the model state and error covariance is given by

$$\mathbf{x}_f = \tilde{\mathbf{M}}\mathbf{x} + \boldsymbol{\eta} \quad (17)$$

$$\tilde{\mathbf{P}}_f = \tilde{\mathbf{M}}\tilde{\mathbf{P}}\tilde{\mathbf{M}}^T + \tilde{\mathbf{Q}}. \quad (18)$$

[55] The operator $\tilde{\mathbf{M}}$ is the full nonlinear operator that represents the transition from one time step to the next of the first-principle physics model. The error on the model prediction is given by $\boldsymbol{\eta}$, and the model error covariance is given by $\tilde{\mathbf{Q}}$. To solve equation (18) exactly requires a computationally prohibitive number of full nonlinear forward model runs. To make the problem tractable, the full physics model is linearized about some reference state. Then $\tilde{\mathbf{M}}$ becomes a linear matrix on the reduced-state grid. This reduced-state approach was tested under simulation [Scherliess et al., 2004], though for the simulation only the predictions of electron density obtained from the first-principle model (with driver adjustment) were used. The full analyzed electron density and error covariance (such as obtained from IDA3D, equations (12) and (13)) was not used in the simulation. The results of the simulation are presented in Figure 1.

[56] The Global Assimilative Ionospheric Model (GAIM) has been under development by the University of Southern California and the Jet Propulsion Laboratory [Wang et al., 2004; Hajj et al., 2004; Pi et al., 2003]. Both a Kalman filter and a four-dimensional variational (4DVAR) technique are included in the USC/JPL GAIM algorithms. The Kalman filter is very similar to the USU approach described already and will not be discussed further. Here the focus is on the 4DVAR approach to data assimilation. In 4DVAR the idea is to use measurements over some range of times to estimate both the initial state of the ionosphere and the input drivers to a first-principle ionospheric model. The USC/JPL physics model is derived from the University of Sheffield

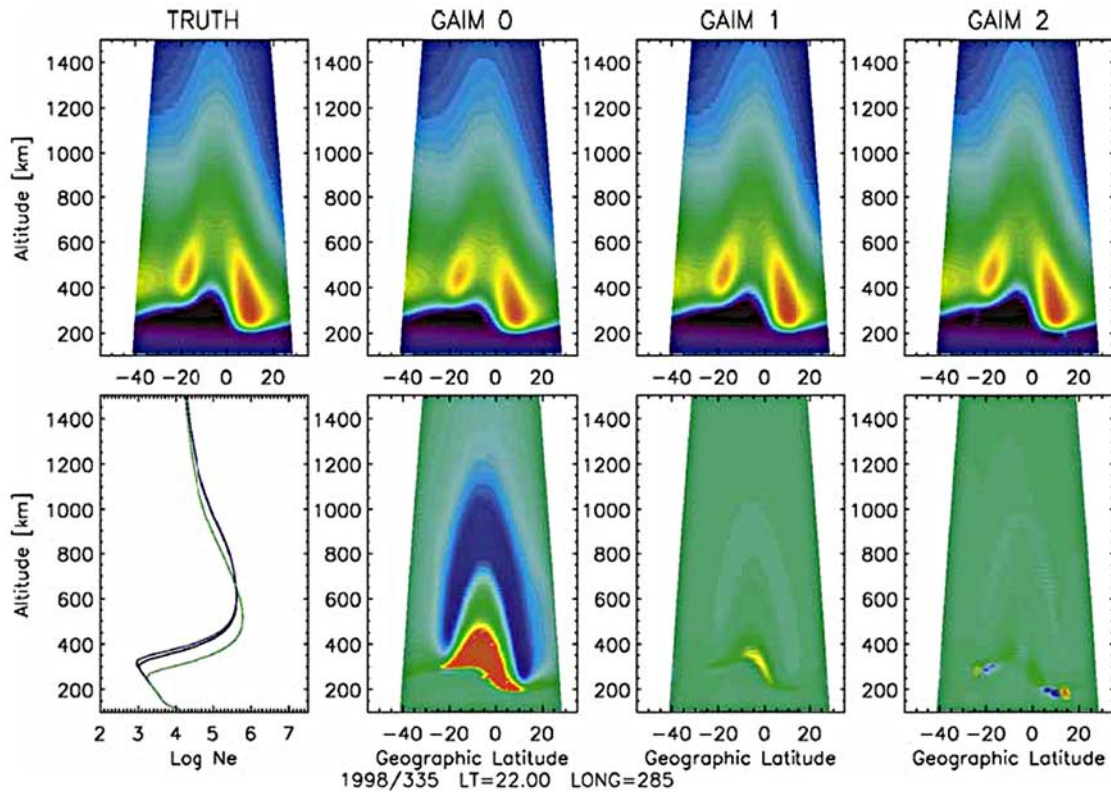


Figure 1. USU GAIM Image [from Scherliess *et al.*, 2004].

model [Bailey *et al.*, 1997]. However, it considers only a single ion species O⁺. It solves the ion continuity and momentum equations, but it ignores the time variation and inertial terms in the momentum equation. The ion momentum equation is further broken into a field-parallel and field-perpendicular component. The velocity component perpendicular to the magnetic field is considered to be due entirely to $\mathbf{E} \times \mathbf{B}$ and is an input driver. The parallel component of velocity also has input drivers due to neutral winds and electron and ion temperatures. Thus the only state variable solved for is the O⁺ density; the rest are input drivers to the system. These driver inputs must be obtained from empirical models including the following: thermospheric densities from the Mass Spectrometer Incoherent Scatter model [Hedin, 1991], neutral winds from the horizontal wind model [Hedin *et al.*, 1996], solar EUV as described by Tobiska [1991], electric fields [e.g., Fejer, 1991; Heppner and Maynard, 1987; Scherliess and Fejer, 1999], and electron energy precipitation flux [Fuller-Rowell and Evans, 1987]. A 4DVAR estimation algorithm for the O⁺ model described above was implemented by the USC/JPL group. Following Pi *et al.* [2003], the cost function to be minimized is given as

$$J(\mathbf{x}_0, \mathbf{a}) = \sum_k^N \|\mathbf{y}_k - \mathbf{H}_k \mathbf{x}_k\| + \gamma_n \|\mathbf{x}_0 - \mathbf{x}_{\text{apriori}}\| + \gamma_F \cdot \|\mathbf{a} - \mathbf{a}_{\text{apriori}}\|, \quad (19)$$

with k referring to time t_k . The notation is the same as described in (13)–(16), with the exception that \mathbf{x}_0 now refers to the electron density distribution at time 0. The input drivers are represented through the vector of unknown parameters \mathbf{a} . The parameters γ_n and γ_F are regularization factors. The a priori designation refers to the initial guess or background values for the O⁺ density and the input drivers. To minimize J , a nonlinear estimator such as the quasi-Newton method is used. However, a major challenge is the calculation of the gradient of J for every parameter to be solved for. The solution is to construct an adjoint equation and propagate the solution backward in time from the measurement time to the initial time t_0 . The math is not repeated here. The interested reader can refer to Pi *et al.* [2003] and references therein. In principle, self-consistent estimation of the initial state and driving parameters will provide an accurate estimation of the O⁺. However, to date, only simulation experiments have been reported in the literature. Simulation in this case means setting up a computer model to test the feasibility of new technique. One such experiment was conducted in 2003 [Pi *et al.*, 2003]. In the 2003 experiment, only vertical drift at the geomagnetic equator was simulated and estimated, while all the other inputs were held at their empirical values. The vertical drift was parameterized by nine coefficients at different local times. For such a small set of unknowns the simulated results were promising (Figure 2). This was then followed by another simulation experiment in 2004 [Pi *et al.*, 2004] where both the vertical drift and neutral winds

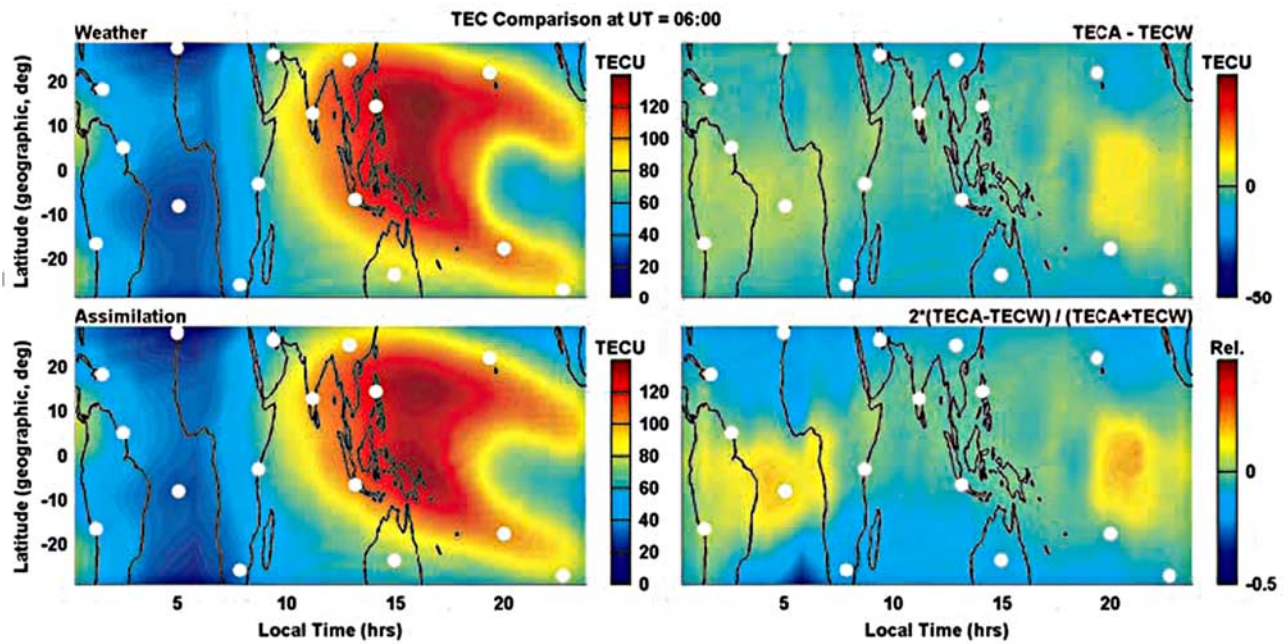


Figure 2. USC/JPL GAIM Image [from *Pi et al.*, 2003].

were solved for. Actual experiments that validate against independent measurements of plasma density or driving parameters have not yet been reported in the literature, although *Mandrake et al.* [2005] show promising comparisons with other sources of TEC for the Kalman filter version of GAIM.

4. EARLY RESULTS AND EXPERIMENTAL VALIDATION OF IONOSPHERIC IMAGING

[57] Experiments in ionospheric tomography have been conducted since the early 1990s. The receiver configurations depend on the choice of satellite system: In the case of NIMS the satellites are in geographic polar orbit, and hence the receivers are placed close to lines of constant geographic longitude, whereas the for the Cicada satellites the configuration is for the corresponding geomagnetic coordinates. Both satellite systems are equally useful for ionospheric imaging from geometrical standpoints. In either case it is necessary to find suitable receiver sites on the ground to provide an approximate longitudinal line for the imaging. It should be noted, though, that an ideal latitude-altitude plane can never be achieved in practice because of the Earth rotation under the satellite pass and because the approximations must be made to project the measurements into a 2-D image plane regardless of where that plane is.

[58] Early experimental work was conducted through short-duration campaigns with manned receivers. By the mid to late 1990s these campaigns were largely replaced by permanent deployments of networked receivers. Early experimental results, particularly those that included validation, are described below.

[59] The first experimental result showing a tomographic image of the ionosphere was published by *Andreeva* [1990].

These authors, from the Moscow State University, used TEC data collected at three receivers located at Murmansk (68.6°N, 31.8°E), Kem (65.0°N, 34.6°E), and Moscow (55.7°N, 37.6°E). Their images were reconstructed using an iterative algorithm that operated on relative TEC data. *Pryse and Kersley* [1992] from the University of Wales, Aberystwyth, used TEC measurements collected by receivers in Scandinavia at Kiruna (68.7°N, 20.4°E) and Oulu (65.0°N, 25.5°E) to reconstruct the ionospheric electron density for a satellite pass recorded on 4 September 1986. This was the first tomographic image of the ionosphere to be verified by another instrument. The European Incoherent Scatter (EISCAT) radar made coordinated measurements of electron density in the geographic meridian of Tromsø. The tomographic image showed a northward gradient in electron density in broad agreement with that measured by the radar. A special tomography campaign was carried out in the United Kingdom during December 1990 [*Pryse et al.*, 1993] with receivers placed along a meridional chain at four sites: Lerwick (60.2°N, 1.1°W), Aberdeen (57.2°N, 2.2°W), Hawick (55.4°N, 2.8°W), and Aberystwyth (52.5°N, 4.1°W). Good agreement was found between f_oF_2 measurements from the ionosonde and the corresponding values obtained from the tomographic images. Tomographic images from eight consecutive satellite passes showed the expected behavior of the midlatitude trough, demonstrating the potential of tomography to image large-scale ionospheric structures.

[60] *Kersley et al.* [1993] presented results from the first EISCAT radar observing program specifically designed to provide an independent electron density comparison with tomographic images. The EISCAT radar was run in a meridional scanning mode, and additional information about the height of the layer peak and the electron density was available from ionosondes in Scandinavia. As the IRI

model allowed the direct incorporation of this ionosonde data, it was used as a background ionosphere, and *Kersley et al.* [1993] concluded that the incorporation of ionosonde data resulted in a significant improvement in the tomographic images.

[61] *Kunitsyn et al.* [1994a] presented an overview of the various tomographic methods employed by Russian ionospheric tomographers and presented results from their various tomographic techniques, although no independent measurements were available to verify their images. A further publication by *Kunitsyn et al.* [1994b] contrasted the merits of phase difference as opposed to calibrated phase values as input for the tomographic algorithm. Phase difference refers to the process of taking the difference between the differential phases measured along adjacent raypaths. They described the problem of isolating the initial phase offset for each station. Their results suggested that the determination of the initial phase offset, which enables the subsequent use of absolute TEC, was particularly difficult in the case of strong horizontal gradients in electron density. This confirmed the ideas of *Leitinger et al.* [1975]. They also concluded that the phase difference technique should be more sensitive to the reconstruction of localized electron density disturbances in the ionosphere than methods using calibrated TEC values.

[62] In late 1993 a joint Russian-American tomography experiment was held in the eastern United States and Canada [*Foster et al.*, 1994]. Receivers were placed at four sites located approximately along the 72°W meridian from Rhode Island, United States (41.4°N), to Roberval, Quebec, Canada (48.8°N). Radio transmissions were monitored from both the NNSS and the Russian Cicada satellites. The phase data, collected by both Russian and American receivers, were analyzed independently by the respective research groups. The Millstone Hill incoherent scatter radar (42.6°N, 288.5°E) was operated in an elevation scan mode in the plane of the receivers, and the resulting electron density measurements were used as a comparison to the tomographic images. The Russian tomographic images were produced using a horizontally stratified ionosphere as a background, whereas the American group used the method described by *Raymund et al.* [1994] in conjunction with the parameterized ionospheric model [*Daniell*, 1991] to create the background ionosphere. The results contained measurements recorded during a geomagnetic storm. In one example, depleted ionization between 44° and 66°N was imaged in the Cicada reconstruction and in the radar observations.

[63] *Markkanen et al.* [1995] described a new reconstruction method based on a Bayesian approach. They presented simulated results in which several different peak heights were put into the reconstruction process as a priori information, and the effect of this information on the resulting tomographic images was investigated. The application of this new method to an experimental situation was then tested using data from the Cicada satellites. Measurements were recorded at a chain of four satellite receivers in Scandinavia from Tromsø in Norway to Nurmijävi in Finland. Two tomographic images were produced, one of

which was shown to compare reasonably well with an electron density profile from the EISCAT radar. However, the ambiguity in the vertical profile was not solved, and the selection of the peak height remained an outstanding problem.

[64] Several other experimental tomographic results were published in a special issue of *Annales Geophysicae*. *Kunitake et al.* [1995] used a modified version of singular value decomposition to reconstruct the electron density over Japan. This extension of SVD involves the truncation of the smaller singular values to remove small-scale perturbations and noise from the data. It also allows the direct incorporation of other constraints into the algorithm and requires no background ionosphere. Other ionospheric information was provided by ionosondes and oblique sounders, which allowed verification of the tomographic images. The results were encouraging, with good agreement found between the peak electron density in tomographic images and ionosonde f_oF_2 values.

[65] *Mitchell et al.* [1995] presented tomographic images of field-aligned irregularities from TEC data collected at the chain of four receivers (Tromsø, Kiruna, Lycksele, and Uppsala) on mainland Scandinavia and one additional station at Ny Ålesund (78.9°N, 12.0°E). To reconstruct the images, the MART algorithm was used with a background ionosphere obtained from the IRI-90 model. The reconstructions showed a latitudinally narrow trough, with a boundary blob on its poleward wall of latitudinal extent around 50 km. The EISCAT radar provided verification of the electron density distribution in the images, confirming the accuracy of the tomographic method (Figure 3). The tomographic images also revealed the signature of auroral E in a tomographic image showing enhanced electron densities beneath the poleward wall of the trough. Further details about experimental results from NIMS imaging can be found in a review paper by *Bernhardt et al.* [1998].

5. SCIENTIFIC RESULTS

5.1. High Latitudes

[66] The high-latitude ionosphere has been studied rather extensively using ionospheric imaging. Tomography is a useful technique for this remote region where sites for instrumentation are sparse and the combination of data from different sources can be useful. In addition, the physics is complex, and scientific studies can benefit from the interpretation of results from multiple instruments. Ionospheric imaging has proved a useful complement to other observations in the auroral regions and the polar cap. Two techniques that have been used with high-latitude ionospheric imaging are outlined below.

[67] Incoherent scatter radars are large, sophisticated instruments for investigating processes in the ionosphere [*Beynon and Williams*, 1978]. They operate by line-of-site scatter from the plasma and thus can view an ionospheric region spanning several hundred kilometers from their location. Such facilities exist at several high-latitude locations and have been used for both verification and for

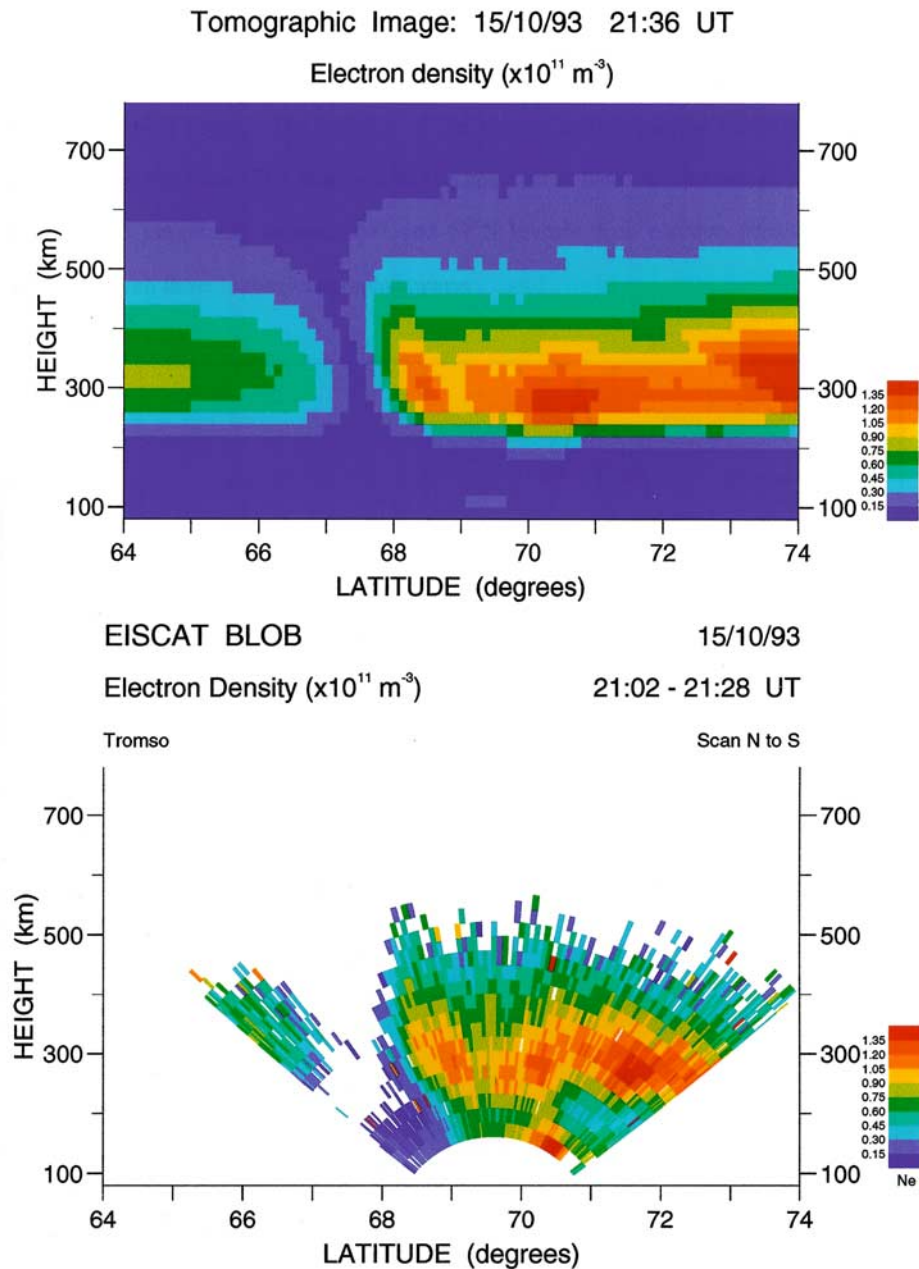


Figure 3. Tomographic image and EISCAT verification. Reprinted from *Mitchell et al.* [1995], with permission.

complementary physical studies with ionospheric imaging. High-latitude ISR facilities include Sondrestrom in Greenland, EISCAT in northern Scandinavia, the EISCAT Svalbard Radar (ESR) on Svalbard, and Irkutsk in Russia. A new redeployable facility, Advanced Modular Incoherent Scatter Radar, is currently active at Fairbanks, Alaska. ISRs have been very important in ionospheric physics because they provide a wealth of information about the ionosphere such as density, temperature, and velocity of the medium. This can be important for the interpretation of ionospheric images [Meggs *et al.*, 2005] by helping to distinguish between processes that change the bulk electron density within a region, such as precipitation and convection.

[68] The Super Dual Auroral Radar Network is a network of HF backscatter radars that is used to form velocity maps of the plasma convection in the polar regions [Greenwald *et al.*, 1995]. This information is a useful complement to ionospheric imaging because it can help to identify the large-scale movement of the plasma. In fact, it can also provide assistance in “static” imaging as it can identify cases where the plasma is convecting at high velocity and may induce image blurring.

[69] The first attempts to use tomographic imaging to investigate the morphology of the ionosphere [Afraimovich *et al.*, 1992] were made soon after the technique first appeared. Since many of the early experimental campaigns

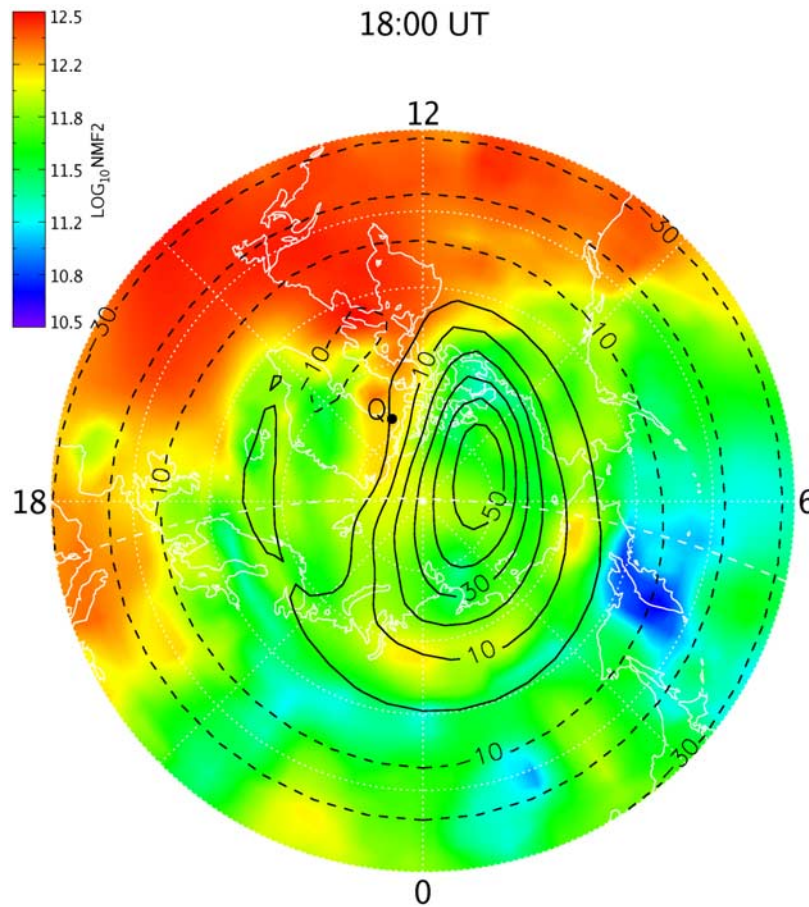


Figure 4. Map of $N_m F_2$ revealing the formation of polar cap patches [from *Bust and Crowley*, 2007].

were located at high latitudes, both auroral and polar cap processes have been investigated, particularly in the European sector [*Mitchell et al.*, 1995; *Walker et al.*, 1996; *Pryse et al.*, 1997; *Walker et al.*, 1998; *Moen et al.*, 1998; *Idenden et al.*, 1998; *Pryse et al.*, 1998a; *Mitchell et al.*, 1998; *Watermann et al.*, 2002]. A variety of structures have been imaged: auroral E layer, nighttime field-aligned irregularities formed from soft particle precipitation, dayside and nightside auroral arcs, and polar cap patches. Both auroral E ionization and a field-aligned irregularity on the poleward wall of the trough are evident in Figure 3.

[70] The origins of polar cap patches have been investigated over the last decade by various researchers using tomographic imaging. Early results used images to reveal high-density plasma structures over Svalbard [*Pryse et al.*, 1997]. *Walker et al.* [1999] demonstrated that particle precipitation in the cusp (dayside) enhanced the plasma density sufficiently to create a structure that subsequently convected into the polar cap as a patch. *Watermann et al.* [2002] revealed polar cap patches convecting across the polar region and warned against the misinterpretation of polar cap plasma in static tomographic imaging when the structures are moving at high velocity. *Sims et al.* [2005] show an example where multi-instrument studies reveal that the plasma can be drawn in from subauroral latitudes. *Stolle et al.* [2005] show patch convection under storm conditions where the interplanetary magnetic field is strongly south-

ward. *Bust and Crowley* [2007] combined a trajectory analysis with a model of the polar cap convection with their imaging to reveal patches being formed from solar radiation building up the plasma density on the dayside of both convection cells. Figure 4 presents an example of using IDA3D imaging to investigate the transport of polar cap patches. Figure 4 reveals a tongue of ionization extending from the noon sector over the polar cap. The convection pattern was obtained from the assimilative mapping ionospheric electrodynamics algorithm. “Q” in Figure 4 denotes the location of Qaanaaq. In addition to the tongue of ionization it also appears as if plasma is being convected from the morning sector toward noon where the solar radiation increases the plasma density as it convects past noon and back toward the midnight sector. These studies have shown that polar cap plasma can arise both from convected precipitation-produced plasma and from solar-produced plasma, which itself can originate at both polar and subauroral latitudes.

[71] Auroral structures have been studied with tomographic imaging since 1995, when *Mitchell et al.* [1995] showed the ability of tomography to image the trough, a field-aligned boundary blob, and auroral E ionization. *Heaton et al.* [1996] showed a trough in the Southern Hemisphere, revealing the first tomographic images in Antarctica. *Kersley et al.* [1997] showed a variety of tomographic images of the trough at U.K. and Scandinavian

latitudes and suggested that tomographic imaging could be a new tool for investigating the trough and creating new models. *Mitchell et al.* [1999] created a large database of U.K. tomographic images and used them to show that previous models of the trough, dependent on geomagnetic indices, could be improved upon by including a seasonal term. *Pryse et al.* [1998b] used tomographic images from a 2-week campaign to reveal the dayside trough at the edge of the convection cell. *Mitchell et al.* [1998] published a multi-instrument study of the dayside auroral ionosphere where an auroral arc was observed in both ESR and tomography. More recently, further trough studies have appeared; *Yizengaw and Moldwin* [2005] have shown the collocation of the trough seen in tomographic imaging with the plasmopause, thus confirming its location on the boundary between open and closed geomagnetic field lines. *Voiculescu et al.* [2006] conducted a statistical study of the main trough and found that the interplanetary magnetic field (IMF) plays a role in the occurrence of the trough at different levels of geomagnetic activity. They also confirmed the importance of the season in the trough location. Thus tomographic imaging has been useful in revealing ionization at low altitudes from auroral *E*, *F* layer field-aligned blobs, and the main trough and has been able to provide a new insight to identify important factors for modeling of the trough, namely, season and IMF.

5.2. Midlatitudes

[72] In 1995 a special issue of *Annales Geophysicae* contained several papers on ionospheric tomography. Three of these papers presented experimental results showing tomographic images of traveling ionospheric disturbances (TIDs) [*Cook and Close*, 1995; *Markkanen et al.*, 1995; *Pryse et al.*, 1995]. These wave-like structures are the manifestation of internal atmospheric gravity waves in the ionosphere. *Pryse et al.* presented results showing medium-scale TIDs obtained during an extended experimental campaign, lasting some 7 months, held in the United Kingdom in 1992–1993. Tomographic images of these features from successive satellite passes allowed the meridional component of the wavelengths and southward velocities to be found. *Cook and Close* also presented several images of TIDs from data recorded during the Mid-America Computerized Ionospheric Tomography Experiment (MACE '93) campaign. Subsequent work by *Nygren et al.* [1997] showed the preferential visibility of the structures due to their field-aligned slope.

[73] The response of the ionosphere to large changes in geomagnetic activity is called an ionospheric storm. Ionospheric storms have been observed with TEC, and an excellent review of the findings is given by *Mendillo* [2006]. *Buonsanto et al.* [1997] recognized the need to make a global specification of the ionosphere at storm time and recognized the use of both radio and optical tomographic techniques. The strength of tomographic imaging is that the plasma dynamics can be observed over a large scale. *Bust et al.* [1997] studied a November 1993 storm to reveal a deep equatorward surge of the midlatitude trough to

nearly 50° geomagnetic latitude, while the ionosonde showed dramatic variations in the virtual height of the ionosphere. *Hernández-Pajares et al.* [1998] initiated the use of GPS tomography for studying ionospheric storms. Previous ionospheric storm studies had suffered from a lack of real knowledge about the longitudinal variation of the plasma, and GPS clearly offered a real possibility to observe the large-scale structure of the dynamic and disturbed ionosphere. A number of tomographic studies have been conducted using GPS data from the recent solar maximum. The July 2000 storm revealed dramatic uplifts in the *F* layer height over the mainland United States [*Yin et al.*, 2004] that were confirmed by Millstone Hill ISR. *García-Fernández et al.* [2005] show the use of the SAC-C satellite occultation data in ionospheric imaging. *Yin and Mitchell* [2005] demonstrated the use of the CHAMP satellite occultation data in imaging the April 2002 storm time ionosphere. *Yizengaw and Moldwin* [2005] used tomography to show the trough and thus to demonstrate with other data the collocation of the plasmopause with the trough (Figure 5). *Yizengaw et al.* [2006] revealed a downward plasma drift for the November 2003 storm. More recently, *Yin et al.* [2006] showed a time dependence in the peak height elevations during several storms and discussed the electric field or neutral wind role in this effect. Thus GPS imaging is being used to create a new view of the midlatitude ionosphere, and, in particular, it complements the 2-D GPS mapping [e.g., *Wilson et al.*, 1995] to reveal the 3-D dynamics of the plasma during storms.

5.3. Low Latitudes

[74] At lower latitudes, images of the equatorial anomaly have been produced from the Asian sector [*Huang et al.*, 1997; *Franke et al.*, 2003; *Xu et al.*, 2000a, 2000b; *Tsai et al.*, 2000], from India [*Thampi et al.*, 2004], and from southern Europe [*Materassi et al.*, 2003]. *Huang et al.* [1999] undertook an interesting study into the response of the low-latitude ionosphere during a solar eclipse. Their tomographic results had implications for understanding the ionospheric dynamics in the equatorial anomaly region during the eclipse. *Xu et al.* [2000a] revealed the rapid formation of a depletion in ionization at 10° geomagnetic latitude, where the anomaly peak usually lies, after the commencement of a storm. *Tsai et al.* [2000] have used tomographic imaging to study the seasonal variations of the location, the time of occurrence, and the height and the electron density of the maximum peak of the anomaly. *Andreeva et al.* [2000] showed the anomaly under a variety of geomagnetic conditions and seasons. *Xu et al.* [2000b] demonstrated how tomography can be used to study the day-to-day variability of the anomaly crests and interpreted their results in the light of changing equatorial electrodynamics. *Yeh et al.* [2001] found from their extensive study that the movement of the anomaly crest was about 1° per hour poleward, slowing as it reaches its highest latitude where it remained until weakening and receding in the afternoon. They also found that the crest latitude correlates with the fountain strength. *Kunitsyn et al.* [2003] used

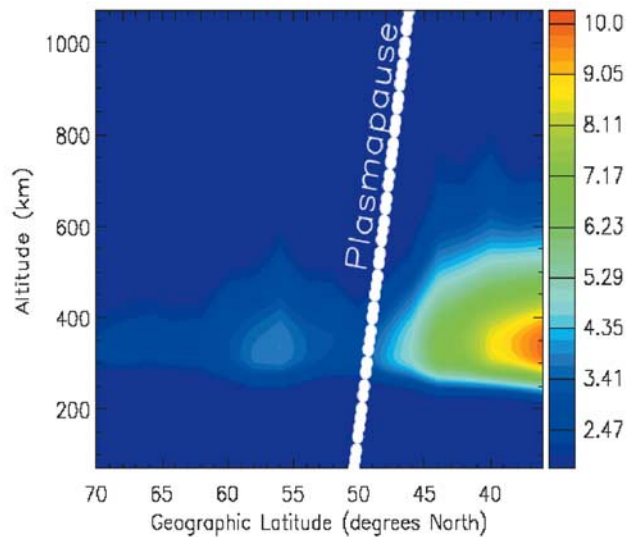


Figure 5. Tomographic image of the trough and the location of the plasmopause [from Yizengaw *et al.*, 2006].

successive images of the anomaly to reveal 2-D electron fluxes.

[75] Huang *et al.* [1995] demonstrated the use of the IRI model in reconstructing the equatorial ionosphere using tomography. Doherty *et al.* [1997] used tomography over the U.S. sector in conjunction with a low-latitude ionosphere model to look at the effects of a storm. Huang *et al.* [1997] used the low-latitude ionospheric tomography network at 121°E to view the diurnal behavior of the ionosphere.

[76] Ledvina *et al.* [2004] demonstrated the first attempts to understand the morphology of the ionosphere in the location of scintillation events using ionospheric imaging. They used a network of GPS TEC receivers in South America and GPS scintillation receivers across Brazil to show that the predominant regions of scintillation are coincident with strong TEC gradients on the edge of the anomaly walls.

[77] Thus ionospheric imaging has been used to study the morphology and dynamics of the equatorial ionosphere on both short and long timescales. The large- and small-scale processes are being related. The results will be useful to improve ionospheric models.

6. APPLICATIONS

[78] Scientific studies of the ionosphere are fundamentally investigations where the objective is to increase and enhance our understanding of the physical world. However, in addition to understanding the ionosphere from a physics standpoint, specification of the electron density in the ionosphere is useful for a number of different applications: communications, navigation, and surveillance. The ionosphere can have two very different effects on communications systems. First, at HF the ionosphere is the medium that refracts signals back to the Earth in over the horizon

communications. The electron density at a given time defines the refractive paths of the signals, and hence knowledge of this is of interest to communications planners. Second, the smaller-scale electron density structures and regions of strong refractive gradients can also be important for communications because the signals can experience diffraction and refraction causing fading known as scintillations as they pass through such regions.

[79] The ionosphere affects satellite navigation systems because the signals experience an unknown time delay as they pass through it that maps into a navigation error. This is a problem for single-frequency systems, such as the GPS L1 navigation signal. To bound and manage this problem, a number of real-time mapping systems have been constructed (e.g., the wide area augmentation system) that continually monitor the ionospheric delay and create and broadcast maps and error estimates to make corrections for the ionospheric errors. Ionospheric tomography has been proposed as a next-generation ionospheric correction for regions where the ionosphere is more complicated, such as the equatorial anomaly regions over South America. Meggs *et al.* [2004] and Meggs and Mitchell [2006] have investigated the gain between 2-D ionospheric mapping and 3-D imaging and found a threefold improvement in TEC mapping using 3-D imaging.

[80] Bust *et al.* [1994] investigated the application of ionospheric tomography to single-site location (SSL) range estimation, the determination of the location of an unknown HF transmitter. An extended campaign known as MACE '93 was held in 1993. Satellite receivers were deployed in two configurations. The first involved nine receivers in a meridional chain stretching from Pierre, South Dakota, to Pharr, Texas, and for the second configuration the receivers were shared between two parallel meridional chains set apart by 5° longitude. The tomographic images were reconstructed using the MART algorithm. Two target transmitters were deployed in Pierre, South Dakota, and Norman, Oklahoma, and the azimuth and elevation of these signals were recorded in San Antonio, Texas. The classical method of SSL range estimation uses an ionosonde to estimate the ionospheric electron density, but Bust *et al.* found that ray tracing through tomographic images produced a statistically smaller error in the range estimates. This was a very encouraging result and showed the promise of tomographic imaging for applications as well as scientific work.

[81] Rogers *et al.* [2001] set up an experiment to image the ionosphere over the United Kingdom and to make coincident measurements with an oblique sounder. Thus the images could be ray traced through and subsequently checked against the oblique paths. The results showed that tomographic images could be used as an aid to HF communications planning.

[82] Ruffini *et al.* [1998] demonstrated that ionospheric imaging could be used to provide an ionospheric calibration for radar altimeters. Hernández-Pajares *et al.* [1999] imaged the ionosphere at European midlatitudes using ground GPS and ionosondes. They demonstrated how a single

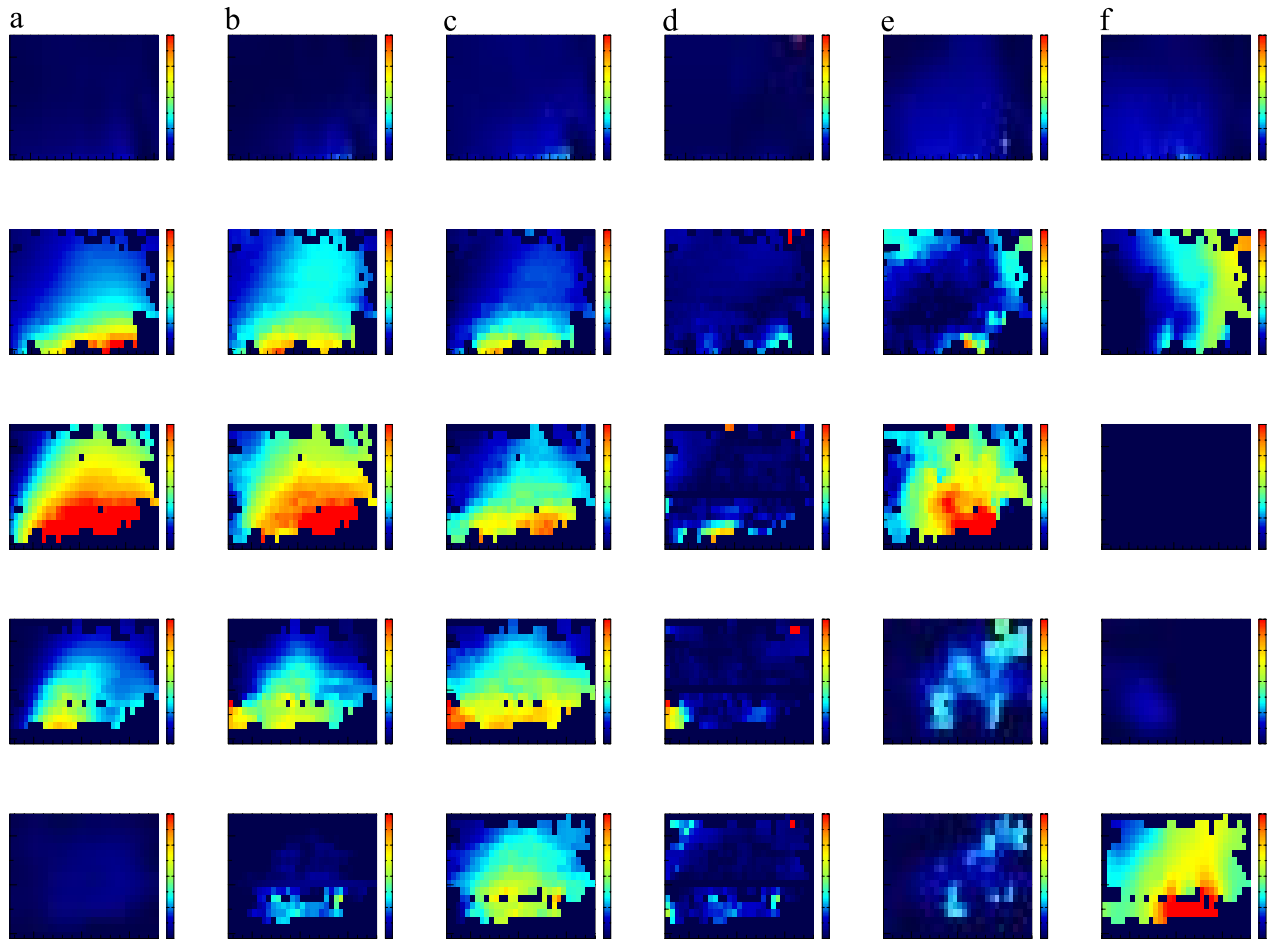


Figure 6. Slices of tomographic images using different instrument combinations. (a) Reference IRI distribution, (b) inversion using semisynthetic GPS data and ionosondes, (c) only semisynthetic GPS, (d) difference between Figures 6b and 6a, (e) result using real GPS and ionosonde data, and (f) only GPS data. The five layer boundary heights are (bottom to top) 75, 125, 175, 250, 650, and 2000 km. Reprinted from *Hernández-Pajares et al.* [1999], with permission from Elsevier.

ionosonde when combined with GPS ground data could provide reliable 3-D images of electron density over 20° of latitude. Figure 6 shows horizontal images at five different heights. The five layer boundary heights are (starting at the bottom) 75, 125, 175, 250, 650, and 2000 km. Figure 6a represents the reference IRI distribution, Figure 6b is the inversion using semisynthetic GPS data and ionosondes, Figure 6c is only the semisynthetic GPS, Figure 6d is the difference between Figures 6b and 6a, Figure 6e is the result using real GPS and ionosonde data, and Figure 6f uses only GPS data. The inversion is for 2 November 1997. This type of quantification of the imaging error is essential for the assessment of ionospheric imaging for many different applications.

[83] *Hernández-Pajares* [2000, 2002] has investigated the application of ionospheric imaging to combine real-time geodetic and ionospheric techniques to achieve a significant improvement in the reliability of carrier phase ambiguity resolution. The model is obtained from the GPS L1 and L2 carrier phase data, and it is used to estimate undifferenced

and double-differenced ionospheric corrections in real time and at very long distances between receivers (500–3000 km). It has been tested under difficult ionospheric conditions during four consecutive weeks in March–April 2001 at solar maximum and at latitudes ranging from -40° to $+40^\circ$ to include the equatorial region. The results are very promising for application to geodetic problems.

7. FUTURE DIRECTIONS

[84] Over the last 20 years, ionospheric tomography has developed from 2-D simulations into 4-D near-global specification of the Earth's ionosphere. New directions for the research are likely to be in several areas: (1) improved electron density values that can be achieved through better algorithms and more data, (2) extension of the imaging to variables other than the electron density, (3) combining tomographic images with models to identify the physical driving parameters for a system, (4) extension of the techniques into other regions of the Earth's environment

and the solar system, and (5) self-consistently combining imaging results at different spatial scales. These ideas are discussed in sections 7.1–7.5.

7.1. Improved 4-D Imaging of Ionospheric Electron Density

[85] While the current algorithms that provide 4-D imaging of ionospheric density are mature, well-validated, and accurate and have been applied to both science and applications, there is a lot of room for improvement. First, the addition of more sensors of measurements than are currently used by 4-D imaging will increase the global data coverage, accuracy, and resolution. These measurements include TEC from the European Space Agency Galileo satellites, increased deployment of new ground-based, inexpensive GPS software receivers, deployments of Digisondes and dynasondes, satellite-based TEC measurements from GPS navigation receiver and GPS occultation measurements, TEC measurements from the Doppler orbitography and radiopositioning integrated by satellite (DORIS) network of ground-based transmitters, cross-link TEC measurements between LEO satellites transmitting on 150 and 400 MHz and the new scintillation and tomography receiver in space (CITRIS) recently launched on STPSat-1, and in situ measurements of electron density from satellites. In addition, new data sets can be incorporated into 4-D imaging algorithms. These data sets generally involve a more complex relationship with the underlying electron density, including nonlinear relationships, and the need to specify auxiliary information. Some of the new data sources being considered for 4-D imaging include EUV observations at 1356 Å, the more basic time delay versus frequency observations obtained from ionograms [Friedman *et al.*, 2006], time delay versus frequency from oblique HF instruments, Riometer absorption data, optical data at 7774 and 6300 Å, and time delay versus frequency from whistlers. Both the Riometer data and the optical 6300 data require specification of auxiliary parameters (collision frequencies and neutral densities), but to the degree that empirical or first-principle models can make good estimates of the auxiliary parameters, these data sources can be used to improve imaging in the *E* region and *F*₁ layer of the ionosphere.

[86] Many of the measurements from these new data sources are nonlinearly related to the electron density. The 1356 EUV data and 7774 optical data are given by a line integral over the square of the electron density (assuming that O⁺ is equal to electron density). Time delay versus frequency measurements from ionograms, HF oblique measurements, and whistlers involve integrals over the refractive index, which is strongly nonlinear and requires ray-tracing methods.

[87] In addition to adding additional data sources, ionospheric 4-D imaging can be improved in several ways. As more data sets become available, higher-resolution spatial images can be made. A reasonable goal is to achieve horizontal resolution of ~10 km and vertical resolution of ~5 km. The horizontal resolution can be achieved by a local dense array of ground instruments such as GPS receivers.

Vertical resolution can be achieved by GPS occultations for a constellation of satellites such as the current constellation observing system for meteorology ionosphere and climate (COSMIC) array. Finally, as more and more data sets become available, the goal is for 4-D imaging algorithms to have less and less reliance on a priori information, with the imaging results only depending on the data.

7.2. Imaging Other Ionospheric and Thermospheric State Variables

[88] Any state variable that can be related to observations through some forward model, and with observations distributed over a large spatial region, can, in principle, be amenable to 4-D imaging methods. For example, a thermospheric variable that could be imaged is neutral composition using optical ground measurements and UV space-based measurements as data sources. In addition, multivariate imaging methods can be developed similar to multivariate objective analysis in meteorology [Daley, 1991]. In multivariate analysis, error cross-covariances between state variables exist, and the cross-covariances allow all observations, both ionospheric and neutral, to influence the state variables. Other possible state variables that could be imaged from observations include neutral winds, temperatures, and ionospheric currents.

7.3. Estimation of Physical Drivers From 4-D Imaging

[89] The idea of combining physical models with tomographic images is a very powerful tool for physical studies. The goal is to extract as much information about the state of the ionosphere system from the imaging as is possible. The 4-D imaging reveals the time-evolving electron density. The next step is to obtain quantitative information on the physical drivers that are producing the time-evolving electron density. This is different from estimating inputs to sophisticated data assimilation algorithms [Pi *et al.*, 2003, 2004; Scherliess *et al.*, 2004]. There, a highly complex, complicated forward model exists between the desired inputs and the measured data, making accurate estimation of the inputs an extremely challenging problem. In 4-D imaging the relationship between the 3-D time-evolving images and the desired physical driver is kept as simple as possible. To take just one example, at high latitudes if the variation in electron density is due primarily to horizontal transport, the imaging can be used to obtain estimates on the plasma drifts caused by the changing electric fields. This could be done by identification of plasma structures in consecutive frames of the imaging and calculating the necessary electric field strengths to convect the plasma using information on the magnetic field strength from a model.

7.4. Imaging of Other Geophysical Systems

[90] Any physical variable that can be related through an integral equation to observables can, in principle, be applied to 4-D imaging. However, sufficient observations are needed over sufficient regions to image accurately the quantity of interest. For other geophysical systems, new and novel ways to take measurements that can be related to underlying

physical variables need to be investigated so that the general methodology of tomographic inverse imaging can be applied to the geophysical problem. Some of the geophysical problems that are open to exploration through 4-D imaging include unexplored Earth regions such as the deep ocean and Antarctica, plasma density throughout the entire solar/magnetosphere/ionosphere, and various geophysical problems on other planets.

7.5. Linking Multiple Scales and/or Different Regions

[91] Imaging of different geophysical regions such as the solar region, magnetosphere, and ionosphere leads to the need to self-consistently couple these different imaged regions into a single coherent picture. Self-consistently combining imaging results at different spatial scales is also desired. For example, ionospheric diffraction tomography acts on irregularities over scales of a few meters to few kilometers. Global 4-D imaging acts over (horizontal) scales ranging from a few tens of kilometers to the globe. A dense network system would image the scales in between global and irregularity scales. These differently scaled imaging systems should all transition self-consistently from one to the other, with large, global imaging providing the initial backgrounds for regional imaging, which then provides the gradients that drives the irregularities.

[92] One method that can be used to couple different spatial regions and scales is the full data assimilation approach discussed in section 3.2. Data assimilation techniques combine data (or imaging results) with first-principle models. It is in theory possible to self-consistently couple the models on different spatial scales and in differing geophysical regions, and, in fact, such efforts are underway. Then, these coupled, self-consistent systems can ingest data from a variety of data sources, spatial regions, and spatial scales, use them to self-consistently update the initial conditions in the coupled system and the physical drivers and then produce self-consistent images of the medium on all scales of interest. Nevertheless, the complexity of this should not be underestimated. It is not simply a matter of increasing the resolution; scales are implicit in the formation of the existing ionospheric models, and in order to change scales and resolutions, models require more physics than they currently contain. It is also possible that our understanding of the linkage between the physics of different scales could be deficient.

[93] At this point, data assimilation can be considered as a general technique to ingest data that itself may include 4-D imaging of any combination of parameters in the Sun-Earth system. There are no longer simple integral forward models relating state variables to observations: The full power of self-consistent first-principle physics models is required to couple all the imaging regions together. The ultimate result of such a coupling is a single 4-D imaging result of the entire Sun-Earth system, involving all variables of interest on all spatial and temporal scales of interest.

[94] **ACKNOWLEDGMENTS.** C.N.M. would like to acknowledge support from the UK research councils EPSRC and

PPARC. G.S.B. acknowledges support from NSF and ONR during the preparation of this manuscript. The authors are grateful to the late K. C. Yeh for originally suggesting the idea of doing ionospheric tomography.

[95] The Editor responsible for this paper was Peter Riley. He thanks Manuel Hernández-Pajares, an anonymous technical reviewer, and an anonymous cross-disciplinary reviewer.

REFERENCES

- Afraimovich, E. L., O. M. Pirog, and A. I. Terekhov (1992), Diagnostics of large-scale structures of the high-latitude ionosphere based on tomographic treatment of navigation satellite signals and of data from ionospheric stations, *J. Atmos. Terr. Phys.*, **54**, 1265–1273.
- Andreeva, E. S. (1990), Radio tomographic reconstruction of ionization dip in the plasma near the Earth, *J. Exp. Theor. Phys. Lett.*, **52**, 142–148.
- Andreeva, E. S., S. J. Franke, K. C. Yeh, and V. E. Kunitsyn (2000), Some features of the equatorial anomaly revealed by ionospheric tomography, *Geophys. Res. Lett.*, **27**, 2465–2468.
- Austen, J. R., S. J. Franke, and C. H. Liu (1988), Ionospheric imaging using computerized tomography, *Radio Sci.*, **23**, 299–307.
- Bailey, G. J., N. Balan, and Y. Z. Su (1997), The Sheffield University plasmasphere ionosphere model—A review, *J. Atmos. Sol. Terr. Phys.*, **59**, 1541–1552.
- Bernhardt, P. A., et al. (1998), Two-dimensional mapping of the plasma density in the upper atmosphere with computerized ionospheric tomography (CIT), *Phys. Plasmas*, **5**, 2010–2021.
- Beynon, W. J. G., and P. J. S. Williams (1978), Incoherent scatter of radio waves from the ionosphere, *Rep. Prog. Phys.*, **41**, 910–956.
- Bilitza, D. (2001), International Reference Ionosphere 2000, *Radio Sci.*, **36**, 261–275.
- Bracewell, R. N. (1956), Strip integration in radio astronomy, *Aust. J. Phys.*, **9**, 198–217.
- Buonsanto, M. J., M. Codrescu, B. A. Emery, C. G. Fesen, T. J. Fuller-Rowell, D. J. Melendez-Alvira, and D. P. Sipler (1997), Comparison of models and measurements at Millstone Hill during the January 24–26, 1993, minor storm interval, *J. Geophys. Res.*, **102**, 7267–7277.
- Bust, G. S., and G. Crowley (2007), Tracking of polar cap patches using data assimilation, *J. Geophys. Res.*, **112**, A05307, doi:10.1029/2005JA011597.
- Bust, G. S., J. A. Cook, G. R. Kronschnabl, C. J. Vasicek, and S. B. Ward (1994), Application of ionospheric tomography to single-site location range estimation, *Int. J. Imaging Syst. Technol.*, **5**, 160–168.
- Bust, G. S., T. L. Gaussiran, and D. S. Coco (1997), Ionospheric observations of the November 1993 storm, *J. Geophys. Res.*, **102**, 14,293–14,304.
- Bust, G. S., D. S. Coco, and J. J. Makela (2000), Combined ionospheric campaign: 1. Ionospheric tomography and GPS total electron count (TEC) depletions, *Geophys. Res. Lett.*, **27**, 2849–2852.
- Bust, G. S., T. W. Garner, and T. L. Gaussiran II (2004), Ionospheric Data Assimilation Three-Dimensional (IDA3D): A global, multisensor, electron density specification algorithm, *J. Geophys. Res.*, **109**, A11312, doi:10.1029/2003JA010234.
- Censor, Y. (1983), Finite series expansion methods, *Proc. IEEE*, **71**, 409–419.
- Ciraolo, L., F. Azpilicueta, C. Brunini, A. Meza, and S. M. Radicella (2007), Calibration errors on experimental slant total electron content (TEC) determined with GPS, *J. Geod.*, **81**(2), 111–120, doi:10.1007/s00190-006-0093-1.
- Coker, C., G. Kronschnabl, D. S. Coco, G. S. Bust, and T. L. Gaussiran (2001), Verification of ionospheric sensors, *Radio Sci.*, **36**, 1523–1529.

- Cook, J. A., and S. Close (1995), An investigation of TID evolution observed in MACE '93 data, *Ann. Geophys.*, **13**, 1320–1324.
- Cornely, P. J. (2003), Flexible Prior Models: Three-dimensional ionospheric tomography, *Radio Sci.*, **38**(5), 1087, doi:10.1029/2002RS002703.
- Crowley, G., et al. (2006), Global thermosphere-ionosphere response to onset of 20 November 2003 magnetic storm, *J. Geophys. Res.*, **111**, A10S18, doi:10.1029/2005JA011518.
- Daley, R. (1991), *Atmospheric Data Analysis*, Cambridge Univ. Press, Cambridge, U. K.
- Daley, R., and E. Barker (2001), NAVDAS: Formulation and diagnostics, *Mon. Weather Rev.*, **129**(4), 869–883.
- Daniell, R. E. (1991), Parameterized real-time ionospheric specification model: PRISM version 1.0, *Tech. Rep. PL-TR-91-2299*, Phillips Lab., Hanscom Air Force Base, Mass.
- Davies, K. (1990), *Ionospheric Radio*, IEE Electromagn. Waves Ser., vol. 31, P. Peregrinus, London.
- Doherty, P. H., D. N. Anderson, and J. A. Klobuchar (1997), Total electron content over the Pan-American longitudes: March–April 1994, *Radio Sci.*, **32**, 1597–1606.
- Fejer, B. G. (1991), Low latitude electrodynamic plasma drifts: A review, *J. Atmos. Terr. Phys.*, **53**, 677–693.
- Foster, J. C., et al. (1994), Russian-American tomography experiment, *Int. J. Imaging Syst. Technol.*, **5**, 148–159.
- Fougere, P. F. (1995), Ionospheric radio tomography using maximum entropy: 1. Theory and simulation studies, *Radio Sci.*, **30**, 429–444.
- Franke, S. J., K. C. Yeh, E. S. Andreeva, and V. E. Kunitsyn (2003), A study of the equatorial anomaly ionosphere using tomographic images, *Radio Sci.*, **38**(1), 1011, doi:10.1029/2002RS002657.
- Fremouw, E. J., J. A. Secan, and B. M. Howe (1992), Application of stochastic inverse-theory to ionospheric tomography, *Radio Sci.*, **27**, 721–732.
- Friedman, S. V., L. J. Nickisch, M. Aiello, and M. Hausman (2006), Real-time reconstruction of the three-dimensional ionosphere using data from a network of GPS receivers, *Radio Sci.*, **41**, RS5S12, doi:10.1029/2005RS003341.
- Fuller-Rowell, T. J., and D. S. Evans (1987), Height-integrated Pedersen and Hall conductivity patterns inferred from the TIROS-NOAA satellite data, *J. Geophys. Res.*, **92**, 7606–7618.
- Garcia-Fernandez, M., A. Saito, J. M. Juan, and T. Tsuda (2005), Three-dimensional estimation of electron density over Japan using the GEONET GPS network combined with SAC-C data and ionosonde measurements, *J. Geophys. Res.*, **110**, A11304, doi:10.1029/2005JA011037.
- Garner, T. W., G. S. Bust, T. L. Gaussiran II, and P. R. Straus (2006), Variations in the midlatitude and equatorial ionosphere during the October 2003 magnetic storm, *Radio Sci.*, **41**, RS6S08, doi:10.1029/2005RS003399.
- Gelb, A. (1974), *Applied Optimal Estimation*, MIT Press, Cambridge, Mass.
- Gordon, R., R. Bender, and G. T. Herman (1970), Algebraic Reconstruction Techniques (ART) for three dimensional electron microscopy and X-ray photography, *J. Theor. Biol.*, **29**, 471–481.
- Greenwald, R. A., et al. (1995), Darn/Superdarn: A global view of the dynamics of high-latitude convection, *Space Sci. Rev.*, **71**, 761–796.
- Hajj, G. A., R. Ibanezmeier, E. R. Kursinski, and L. J. Romans (1994), Imaging the ionosphere with the global positioning system, *Int. J. Imaging Syst. Technol.*, **5**, 174–184.
- Hajj, G. A., B. D. Wilson, C. Wang, X. Pi, and I. G. Rosen (2004), Data assimilation of ground GPS total electron content into a physics-based ionospheric model by use of the Kalman filter, *Radio Sci.*, **39**, RS1S05, doi:10.1029/2002RS002859.
- Hargreaves, J. K. (1995), *The Solar-Terrestrial Environment: An Introduction to Geospace—The Science of the Terrestrial Upper Atmosphere, Ionosphere, and Magnetosphere*, Cambridge Atmos. Space Sci. Ser., vol. 5, Cambridge Univ. Press., New York.
- Heaton, J. A. T., S. E. Pryse, and L. Kersley (1995), Improved background representation, ionosonde input and independent verification in experimental ionospheric tomography, *Ann. Geophys.*, **13**, 1297–1302.
- Heaton, J. A. T., G. O. L. Jones, and L. Kersley (1996), Toward ionospheric tomography in Antarctica: First steps and comparison with dynasonde observations, *Antarct. Sci.*, **8**, 297–302.
- Hedin, A. E. (1991), Extension of the MSIS thermosphere model into the middle and lower atmosphere, *J. Geophys. Res.*, **96**, 1159–1172.
- Hedin, A. E., et al. (1996), Empirical wind model for the upper, middle and lower atmosphere, *J. Atmos. Terr. Phys.*, **58**, 1421–1447.
- Heppner, J. P., and N. C. Maynard (1987), Empirical high-latitude electric field models, *J. Geophys. Res.*, **92**, 4467–4489.
- Hernández-Pajares, M., J. M. Juan, J. Sanz, and J. G. Sole (1998), Global observation of the ionospheric electronic response to solar events using ground and LEO GPS data, *J. Geophys. Res.*, **103**, 20,789–20,796.
- Hernández-Pajares, M., J. M. Juan, and J. Sanz (1999), New approaches in global ionospheric determination using ground GPS data, *J. Atmos. Sol. Terr. Phys.*, **61**, 1237–1247.
- Hernández-Pajares, M., J. M. Juan, J. Sanz, and O. L. Colombo (2000), Application of ionospheric tomography to real-time GPS carrier-phase ambiguities resolution, at scales of 400–1000 km and with high geomagnetic activity, *Geophys. Res. Lett.*, **27**, 2009–2012.
- Hernández-Pajares, M., J. M. Juan, J. Sanz, and O. L. Colombo (2002), Improving the real-time ionospheric determination from GPS sites at very long distances over the equator, *J. Geophys. Res.*, **107**(A10), 1296, doi:10.1029/2001JA009203.
- Hounsfield, G. N. (1972), A method of and apparatus for examination of a body by radiation such as X-ray or gamma radiation, Patent 1283915, U.S. Patent and Trademark Off., Washington, D. C.
- Howe, B. M., K. Runciman, and J. A. Secan (1998), Tomography of the ionosphere: Four-dimensional simulations, *Radio Sci.*, **33**, 109–128.
- Huang, C. R., C. H. Liu, H. C. Yeh, W. H. Tsai, C. J. Wang, K. C. Yeh, K. H. Lin, and H. L. Tsai (1995), IRI model application in low latitude ionospheric tomography, in *Low and Equatorial Latitudes in the International Reference Ionosphere (IRI)*, edited by K. Rawer et al., pp. 237–240, Elsevier, New York.
- Huang, C. R., C. H. Liu, H. C. Yeh, and W. K. Tsai (1997), The low-latitude ionospheric tomography network (LITN)—Initial results, *J. Atmos. Sol. Terr. Phys.*, **59**, 1553–1567.
- Huang, C. R., C. H. Liu, K. C. Yeh, K. H. Lin, W. H. Tsai, H. C. Yeh, and J. Y. Liu (1999), A study of tomographically reconstructed ionospheric images during a solar eclipse, *J. Geophys. Res.*, **104**, 79–94.
- Idenden, D. W., R. J. Moffett, M. J. Williams, P. S. J. Spencer, and L. Kersley (1998), Imaging of structures in the high-latitude ionosphere: Model comparisons, *Ann. Geophys.*, **16**, 969–973.
- Juan, J. M., A. Rius, M. Hernández-Pajares, and J. Sanz (1997), A two-layer model of the ionosphere using global positioning system data, *Geophys. Res. Lett.*, **24**, 393–396.
- Kak, A. C., and M. Slaney (2001), *Principles of Computerized Tomographic Imaging*, Soc. of Ind. and Appl. Math., Philadelphia, Pa.
- Kersley, L., J. A. T. Heaton, S. E. Pryse, and T. D. Raymund (1993), Experimental ionospheric tomography with ionosonde input and EISCAT verification, *Ann. Geophys.*, **11**, 1064–1074.
- Kersley, L., S. E. Pryse, I. K. Walker, J. A. T. Heaton, C. N. Mitchell, M. J. Williams, and C. A. Willson (1997), Imaging of electron density troughs by tomographic techniques, *Radio Sci.*, **32**, 1607–1621.

- Kivelson, M. G., and C. T. Russell (1995), *Introduction to Space Physics*, Cambridge Univ. Press, New York.
- Kuklinski, W. S. (1997), Ionospheric tomography via iterative cross-entropy minimization, *Radio Sci.*, **32**, 1037–1049.
- Kunitake, M., K. Ohtaka, T. Maruyama, M. Tokumaru, A. Morioka, and S. Watanabe (1995), Tomographic imaging of the ionosphere over Japan by the modified truncated SVD method, *Ann. Geophys.*, **13**, 1305–1310.
- Kunitsyn, V. E., E. S. Andreeva, O. G. Razinkov, and E. D. Tereshchenko (1994a), Phase and phase-difference ionospheric radio tomography, *Int. J. Imaging Syst. Technol.*, **5**, 128–140.
- Kunitsyn, V. E., E. S. Andreeva, E. D. Tereshchenko, B. Z. Khudukon, and T. Nygren (1994b), Investigations of the ionosphere by satellite radiotomography, *Int. J. Imaging Syst. Technol.*, **5**, 112–127.
- Kunitsyn, V. E., E. S. Andreeva, A. Y. Popov, and O. G. Razinkov (1995), Methods and algorithms of ray radiotomography for ionospheric research, *Ann. Geophys.*, **13**, 1263–1276.
- Kunitsyn, V. E., E. S. Andreeva, S. J. Franke, and K. C. Yeh (2003), Tomographic investigations of temporal variations of the ionospheric electron density and the implied fluxes, *Geophys. Res. Lett.*, **30**(16), 1851, doi:10.1029/2003GL016908.
- Leitinger, R., G. Schmidt, and A. Tauriainen (1975), An evaluation method combining the differential Doppler measurements from two stations that enables the calculation of the electron content of the ionosphere, *J. Geophys.*, **41**, 201–213.
- Leitinger, R., H. P. Ladreiter, and G. Kirchengast (1997), Ionosphere tomography with data from satellite reception of Global Navigation Satellite System signals and ground reception of Navy Navigation Satellite System signals, *Radio Sci.*, **32**, 1657–1669.
- Ledvina, B. M., P. M. Kintner, and J. J. Makela (2004), Temporal properties of intense GPS L1 amplitude scintillations at midlatitudes, *Radio Sci.*, **39**, RS1S18, doi:10.1029/2002RS002832.
- Lent, A. (1997), A convergent algorithm for maximum entropy image restoration, with a medical X-ray application, in *SPSE Conference Proceedings*, edited by R. Shaw, pp. 249, Soc. of Photogr. Sci. and Eng., Washington, D. C.
- Mandrake, L., B. Wilson, C. Wang, G. Hajj, A. Mannucci, and X. Pi (2005), A performance evaluation of the operational Jet Propulsion Laboratory/University of Southern California Global Assimilation Ionospheric Model (JPL/USC GAIM), *J. Geophys. Res.*, **110**, A12306, doi:10.1029/2005JA011170.
- Mannucci, A. J., B. Iijima, L. Sparks, X. Q. Pi, B. Wilson, and U. Lindqwister (1999), Assessment of global TEC mapping using a three-dimensional electron density model, *J. Atmos. Sol. Terr. Phys.*, **61**, 1227–1236.
- Markkanen, M., M. Lehtinen, T. Nygren, J. Pirttila, P. Henelius, E. Valenius, E. D. Tereshchenko, and B. Z. Khudukon (1995), Bayesian approach to satellite radiotomography with applications in the Scandinavian sector, *Ann. Geophys.*, **13**, 1277–1287.
- Materassi, M., and C. N. Mitchell (2005a), A simulation study into constructing of the sample space for ionospheric imaging, *J. Atmos. Sol. Terr. Phys.*, **67**, 1085–1091.
- Materassi, M., and C. N. Mitchell (2005b), Imaging of the equatorial ionosphere, *Ann. Geophys.*, **48**(3), 477–482.
- Materassi, M., C. N. Mitchell, and P. S. J. Spencer (2003), Ionospheric imaging of the northern crest of the equatorial anomaly, *J. Atmos. Sol. Terr. Phys.*, **65**, 1393–1400.
- McNamara, L. P. (1991), *Ionosphere: Communications, Surveillance and Direction Finding*, Krieger, Malabar, Fla.
- Meggs, R. W., and C. N. Mitchell (2006), A study into the errors in vertical total electron content mapping using GPS data, *Radio Sci.*, **41**, RS1008, doi:10.1029/2005RS003308.
- Meggs, R. W., C. N. Mitchell, and P. S. J. Spencer (2004), A comparison of techniques for mapping total electron content over Europe using GPS signals, *Radio Sci.*, **39**, RS1S10, doi:10.1029/2002RS002846.
- Meggs, R. W., C. N. Mitchell, and V. S. C. Howells (2005), Simultaneous observations of the main trough using GPS imaging and the EISCAT radar, *Ann. Geophys.*, **23**, 753–757.
- Mendillo, M. (2006), Storms in the ionosphere: Patterns and processes for total electron content, *Rev. Geophys.*, **44**, RG4001, doi:10.1029/2005RG000193.
- Menerbo, G. (1979), MENT: A maximum entropy algorithm for reconstructing a source from projection data, *Comput. Graphics Image Process.*, **10**, 48–68.
- Mitchell, C. N. (2002), Imaging of near-Earth space plasma, *Philos. Trans. R. Soc. London, Ser. A*, **360**, 2805–2818.
- Mitchell, C. N., and P. S. J. Spencer (2003), A three-dimensional time-dependent algorithm for ionospheric imaging using GPS, *Ann. Geophys.*, **46**, 687–696.
- Mitchell, C. N., D. G. Jones, L. Kersley, S. E. Pryse, and I. K. Walker (1995), Imaging of field-aligned structures in the auroral ionosphere, *Ann. Geophys.*, **13**, 1311–1319.
- Mitchell, C. N., S. E. Pryse, L. Kersley, and I. K. Walker (1997a), The correction for the satellite-receiver longitude difference in ionospheric tomography, *J. Atmos. Sol. Terr. Phys.*, **59**, 2077–2087.
- Mitchell, C. N., L. Kersley, and S. E. Pryse (1997b), The effects of receiver location in two-station experimental ionospheric tomography, *J. Atmos. Sol. Terr. Phys.*, **59**, 1411–1415.
- Mitchell, C. N., L. Kersley, J. A. T. Heaton, and S. E. Pryse (1997c), Determination of the vertical electron-density profile in ionospheric tomography: Experimental results, *Ann. Geophys.*, **15**, 747–752.
- Mitchell, C. N., I. K. Walker, S. E. Pryse, I. Kersley, I. W. McCrea, and T. B. Jones (1998), First complementary observations by ionospheric tomography, the EISCAT Svalbard radar and the CUTLASS HF radar, *Ann. Geophys.*, **16**, 1519–1522.
- Mitchell, C. N., L. Kersley, S. E. Pryse, C. A. Willson, J. A. T. Heaton, P. S. Cannon, and N. C. Rogers (1999), Imaging and modelling of the main ionospheric trough using radio tomography, in *IEEE National Conference on Antennas and Propagation*, **31 March–1 April 1999**, *IEEE Conf. Publ.*, **461**, 192–195.
- Moen, J., S. T. Berry, L. Kersley, and B. Lybekk (1998), Probing discrete auroral arcs by ionospheric tomography, *Ann. Geophys.*, **16**, 574–582.
- Na, H., and H. Lee (1990), Resolution analysis of tomographic reconstruction of electron density profiles in the ionosphere, *Int. J. Imaging Syst. Technol.*, **2**, 209–218.
- Na, H., and E. Sutton (1994), Resolution analysis of ionospheric tomography systems, *Int. J. Imaging Syst. Technol.*, **5**, 169–173.
- Na, H., J. Shen, and H. Lee (1995), A Fourier domain technique for ionospheric tomography, *Radio Sci.*, **30**, 747–754.
- Nygren, T., M. Markkanen, M. Lehtinen, E. D. Tereshchenko, and B. Z. Khudukon (1997), Stochastic inversion in ionospheric radiotomography, *Radio Sci.*, **32**, 2359–2372.
- Pi, X., C. Wang, G. A. Hajj, G. Rosen, B. D. Wilson, and G. J. Bailey (2003), Estimation of $\mathbf{E} \times \mathbf{B}$ drift using a global assimilative ionospheric model: An observation system simulation experiment, *J. Geophys. Res.*, **108**(A2), 1075, doi:10.1029/2001JA009235.
- Pi, X. Q., C. Wang, G. A. Hajj, G. Rosen, B. D. Wilson, and A. J. Mannucci (2004), Assimilative modeling of low-latitude ionosphere, paper presented at 2004 IEEE Position, Location and Navigation Symposium—PLANS 2004, Monterey, Calif., 26–29 April.
- Pryse, S. E., and L. Kersley (1992), A preliminary experimental test of ionospheric tomography, *J. Atmos. Sol. Terr. Phys.*, **54**, 1007–1012.
- Pryse, S. E., L. Kersley, D. L. Rice, C. D. Russell, and I. K. Walker (1993), Tomographic imaging of the ionospheric midlatitude trough, *Ann. Geophys.*, **11**, 144–149.
- Pryse, S. E., C. N. Mitchell, J. A. T. Heaton, and L. Kersley (1995), Travelling ionospheric disturbances imaged by tomographic techniques, *Ann. Geophys.*, **13**, 1325–1330.

- Pryse, S. E., L. Kersley, M. J. Williams, I. K. Walker, and C. A. Wilson (1997), Tomographic imaging of the polar-cap ionosphere over Svalbard, *J. Atmos. Sol. Terr. Phys.*, **59**, 1953–1959.
- Pryse, S. E., L. Kersley, and M. J. Williams (1998a), Electron density structures in the polar cap imaged by ionospheric tomography, in *Polar Cap Thermosphere/Ionosphere and Its Role in Solar-Terrestrial Physics*, edited by U. P. Lovhaug, *Adv. Space Res.*, **22**(9), 1385–1389.
- Pryse, S. E., L. Kersley, M. J. Williams, and I. K. Walker (1998b), The spatial structure of the dayside ionospheric trough, *Ann. Geophys.*, **16**, 1169–1179.
- Radon, J. (1917), Über die Bestimmung von Funktionen durch ihre Integralwerte längs gewisser mannigfaltigkeiten, *Saechs. Ber. Akad. Wiss.*, **69**, 262–277.
- Raymund, T. D. (1994), Ionospheric tomography algorithms, *Int. J. Imaging Syst. Technol.*, **5**, 75–85.
- Raymund, T. D., J. R. Austen, S. J. Franke, C. H. Liu, J. A. Klobuchar, and J. Stalker (1990), Application of computerized-tomography to the investigation of ionospheric structures, *Radio Sci.*, **25**, 771–789.
- Raymund, T. D., S. E. Pryse, L. Kersley, and J. A. T. Heaton (1993), Tomographic reconstruction of ionospheric electron density with European incoherent scatter radar verification, *Radio Sci.*, **28**, 811–817.
- Raymund, T. D., Y. Bresler, D. N. Anderson, and R. E. Daniell (1994), Model-assisted ionospheric tomography: A new algorithm, *Radio Sci.*, **29**, 1493–1512.
- Rius, A., G. Ruffini, and L. Cucurull (1997), Improving the vertical resolution of ionospheric tomography with GPS occultations, *Geophys. Res. Lett.*, **24**, 2291–2294.
- Roble, R. G., and E. C. Ridley (1994), A thermosphere-ionosphere-mesosphere electrodynamics general circulation model (TIME-GCM): Equinox solar cycle minimum simulations (30–500 km), *Geophys. Res. Lett.*, **21**, 417–420.
- Rogers, N. C., C. N. Mitchell, J. A. T. Heaton, P. S. Cannon, and L. Kersley (2001), Application of radio tomographic imaging to HF oblique incidence ray tracing, *Radio Sci.*, **36**, 1591–1598.
- Ruffini, G., E. Cardellach, A. Flores, L. Cucurull, and A. Rius (1998), Ionospheric calibration of radar altimeters using GPS tomography, *Geophys. Res. Lett.*, **25**, 3771–3774.
- Scherliess, L., and B. G. Fejer (1999), Radar and satellite global equatorial *F* region vertical drift model, *J. Geophys. Res.*, **104**, 6829–6842.
- Scherliess, L., R. W. Schunk, J. J. Sojka, and D. C. Thompson (2004), Development of a physics-based reduced state Kalman filter for the ionosphere, *Radio Sci.*, **39**, RS1S04, doi:10.1029/2002RS002797.
- Schreiner, W. S., S. V. Sokolovskiy, C. Rocken, and D. C. Hunt (1999), Analysis and validation of GPS/MET radio occultation data in the ionosphere, *Radio Sci.*, **34**, 949–966.
- Schunk, R. W., J. J. Sojka, and J. V. Eccles (1997), Expanded capabilities for the ionospheric forecast model, *Rep. AFRLVSH-TR-98-0001*, 1–142, Space Veh. Dir., Hanscom Air Force Base, Mass.
- Schunk, R. W., et al. (2004), Global Assimilation of Ionospheric Measurements (GAIM), *Radio Sci.*, **39**, RS1S02, doi:10.1029/2002RS002794.
- Schunk, R. W., L. Scherliess, J. J. Sojka, D. C. Thompson, and L. Zhu (2005a), An operational data assimilation model of the global ionosphere, pp. 512–581, *Ionospheric Effects Symposium Proceedings*, Natl. Tech. Info. Serv., Springfield, Va.
- Schunk, R., L. Scherliess, J. J. Sojka, D. C. Thompson, and L. Zhu (2005b), Ionospheric weather forecasting on the horizon, *Space Weather*, **3**, S08007, doi:10.1029/2004SW000138.
- Sims, R. W., S. E. Pryse, and W. F. Denig (2005), Spatial structure of summertime ionospheric plasma near magnetic noon, *Ann. Geophys.*, **23**, 25–37.
- Stolle, C., S. Schluter, S. Heise, C. Jacobi, N. Jakowski, S. Friedel, D. Kürschner, and H. Lühr (2005), GPS ionospheric imaging of the north polar ionosphere on 30 October 2003, in *Planetary Atmospheres, Ionospheres, and Magnetospheres*, edited by O. Witaske and M. A. Shea, *Adv. Space Res.*, **36**, 2201–2206.
- Sutton, E., and H. Na (1994), Orthogonal decomposition framework for ionospheric tomography algorithms, *Int. J. Imaging Syst. Technol.*, **5**, 106–111.
- Thampi, S. V., T. K. Pant, S. Ravindran, C. V. Devasia, and R. Sridharan (2004), Simulation studies on the tomographic reconstruction of the equatorial and low-latitude ionosphere in the context of the Indian tomography experiment: CRABEX, *Ann. Geophys.*, **22**, 3445–3460.
- Thompson, D. C., L. Scherliess, J. J. Sojka, and R. W. Schunk (2006), The Utah State University Gauss-Markov Kalman filter of the ionosphere: The effect of slant TEC and electron density profile data on model fidelity, *J. Atmos. Sol. Terr. Phys.*, **68**, 947–958.
- Tobiska, W. K. (1991), Revised solar extreme ultraviolet flux model, *J. Atmos. Terr. Phys.*, **53**, 1005–1018.
- Tsai, W. H., L. F. Huang, M. F. Chen, and C. H. Liu (2000), A tomographic study of seasonal variations of the equatorial anomaly in the Asian sector, *Terr. Atmos. Oceanic Sci.*, **11**, 337–348.
- Vasicek, C. J., and G. R. Kronschnabl (1995), Ionospheric tomography - An algorithm enhancement, *J. Atmos. Terr. Phys.*, **57**, 875–888.
- Voiculescu, M., I. Virtanen, and T. Nygren (2006), The *F*-region trough: Seasonal morphology and relation to interplanetary magnetic field, *Ann. Geophys.*, **24**, 173–185.
- Walker, I. K., J. A. T. Heaton, L. Kersley, C. N. Mitchell, S. E. Pryse, and M. J. Williams (1996), EISCAT verification in the development of ionospheric tomography, *Ann. Geophys.*, **14**, 1413–1421.
- Walker, I. K., J. Moen, C. N. Mitchell, L. Kersley, and P. E. Sandholt (1998), Ionospheric effects of magnetopause reconnection observed using ionospheric tomography, *Geophys. Res. Lett.*, **25**, 293–296.
- Walker, I. K., J. Moen, L. Kersley, and D. A. Lorentzen (1999), On the possible role of cusp/cleft precipitation in the formation of polar-cap patches, *Ann. Geophys.*, **17**, 1298–1305.
- Wang, C., G. Hajj, X. Pi, I. G. Rosen, and B. Wilson (2004), Development of the Global Assimilative Ionospheric Model, *Radio Sci.*, **39**, RS1S06, doi:10.1029/2002RS002854.
- Watermann, J., G. S. Bust, J. P. Thayer, T. Neubert, and C. Coker (2002), Mapping plasma structures in the high-latitude ionosphere using beacon satellite, incoherent scatter radar and ground-based magnetometer observations, *Ann. Geophys.*, **45**, 177–189.
- Wilson, B. D., A. J. Mannucci, and C. D. Edwards (1995), Sub-daily Northern Hemisphere ionospheric maps using an extensive network of GPS receivers, *Radio Sci.*, **30**, 639–648.
- Xu, J. S., S. Y. Ma, X. B. Wu, K. H. Lin, and K. C. Yeh (2000a), Low-latitude ionospheric effects during a moderate storm by tomographic imaging, *Chin. J. Geophys.*, **43**, 145–151.
- Xu, J. S., X. B. Wu, and S. Y. Ma (2000b), Tomographic imaging of ionospheric structures and disturbances in the region of East-Asian equatorial anomaly, *Sci. China, Ser. E*, **43**(4), 395–404.
- Yeh, K. C., and T. D. Raymund (1991), Limitations of ionospheric imaging by tomography, *Radio Sci.*, **26**, 1361–1380.
- Yeh, K. C., S. J. Franke, E. S. Andreeva, and V. E. Kunitsyn (2001), An investigation of motions of the equatorial anomaly crest, *Geophys. Res. Lett.*, **28**, 4517–4520.
- Yin, P., and C. N. Mitchell (2005), Use of radio-occultation data for ionospheric imaging during the April 2002 disturbances, *GPS Solutions*, **9**, 156–163.
- Yin, P., C. N. Mitchell, P. S. J. Spencer, and J. C. Foster (2004), Ionospheric electron concentration imaging using GPS over the USA during the storm of July 2000, *Geophys. Res. Lett.*, **31**, L12806, doi:10.1029/2004GL019899.

Yin, P., C. N. Mitchell, and G. S. Bust (2006), Observations of the *F* region height redistribution in the storm-time ionosphere over Europe and the USA using GPS, *Geophys. Res. Lett.*, *33*, L18803, doi:10.1029/2006GL027125.

Yizengaw, E., and M. B. Moldwin (2005), The altitude extension of the mid-latitude trough and its correlation with plasmopause position, *Geophys. Res. Lett.*, *32*, L09105, doi:10.1029/2005GL022854.

Yizengaw, E., M. B. Moldwin, A. Komjathy, and A. J. Mannucci (2006), Unusual topside ionospheric density response to the November 2003 superstorm, *J. Geophys. Res.*, *111*, A02308, doi:10.1029/2005JA011433.

G. S. Bust, Atmospheric and Space Technology Research Associates, 11118 Quail Pass, San Antonio, TX 78249, USA. (gbust@astraspace.net)

C. N. Mitchell, Department of Electronic and Electrical Engineering, University of Bath, Bath BA2 7AY, UK.